

Substructure dependence of jet cross sections at HERA and determination of α_s

ZEUS Collaboration

Abstract

Jet substructure and differential cross sections for jets produced in the photo-production and deep inelastic ep scattering regimes have been measured with the ZEUS detector at HERA using an integrated luminosity of 82.2 pb^{-1} . The substructure of jets has been studied in terms of the jet shape and subjet multiplicity for jets with transverse energies $E_T^{\text{jet}} > 17 \text{ GeV}$. The data are well described by the QCD calculations. The jet shape and subjet multiplicity are used to tag gluon- and quark-initiated jets. Jet cross sections as functions of E_T^{jet} , jet pseudorapidity, the jet-jet scattering angle, dijet invariant mass and the fraction of the photon energy carried by the dijet system are presented for gluon- and quark-tagged jets. The data exhibit the behaviour expected from the underlying parton dynamics. A value of $\alpha_s(M_Z)$ of $\alpha_s(M_Z) = 0.1176 \pm 0.0009 \text{ (stat.) } \begin{matrix} +0.0009 \\ -0.0026 \end{matrix} \text{ (exp.) } \begin{matrix} +0.0091 \\ -0.0072 \end{matrix} \text{ (th.)}$ was extracted from the measurements of jet shapes in deep inelastic scattering.

The ZEUS Collaboration

S. Chekanov, M. Derrick, J.H. Loizides¹, S. Magill, S. Miglioranzi¹, B. Musgrave, J. Repond,
R. Yoshida

Argonne National Laboratory, Argonne, Illinois 60439-4815, USA ⁿ

M.C.K. Mattingly

Andrews University, Berrien Springs, Michigan 49104-0380, USA

N. Pavel

Institut für Physik der Humboldt-Universität zu Berlin, Berlin, Germany

P. Antonioli, G. Bari, M. Basile, L. Bellagamba, D. Boscherini, A. Bruni, G. Bruni,
G. Cara Romeo, L. Cifarelli, F. Cindolo, A. Contin, M. Corradi, S. De Pasquale, P. Giusti,
G. Iacobucci, A. Margotti, A. Montanari, R. Nania, F. Palmonari, A. Pesci, L. Rinaldi,
G. Sartorelli, A. Zichichi

University and INFN Bologna, Bologna, Italy ^e

G. Aghuzumtsyan, D. Bartsch, I. Brock, S. Goers, H. Hartmann, E. Hilger, P. Irrgang,
H.-P. Jakob, O. Kind, U. Meyer, E. Paul², J. Rautenberg, R. Renner, A. Stifutkin,
J. Tandler³, K.C. Voss, M. Wang

Physikalisches Institut der Universität Bonn, Bonn, Germany ^b

D.S. Bailey⁴, N.H. Brook, J.E. Cole, G.P. Heath, T. Namsoo, S. Robins, M. Wing
H.H. Wills Physics Laboratory, University of Bristol, Bristol, United Kingdom ^m

M. Capua, A. Mastroberardino, M. Schioppa, G. Susinno

Calabria University, Physics Department and INFN, Cosenza, Italy ^e

J.Y. Kim, I.T. Lim, K.J. Ma, M.Y. Pac⁵

Chonnam National University, Kwangju, South Korea ^g

M. Helbich, Y. Ning, Z. Ren, W.B. Schmidke, F. Sciulli

Nevis Laboratories, Columbia University, Irvington on Hudson, New York 10027 ^o

J. Chwastowski, A. Eskreys, J. Figiel, A. Galas, K. Olkiewicz, P. Stopa, L. Zawiejski
Institute of Nuclear Physics, Cracow, Poland ⁱ

L. Adamczyk, T. Bołd, I. Grabowska-Bołd⁶, D. Kisiełewska, A.M. Kowal, M. Kowal, J.
Łukasik, M. Przybycień, L. Suszycki, D. Szuba, J. Szuba⁷

*Faculty of Physics and Nuclear Techniques, AGH-University of Science and Technology,
Cracow, Poland ^p*

A. Kotański⁸, W. Słomiński

Department of Physics, Jagellonian University, Cracow, Poland

V. Adler, U. Behrens, I. Bloch, K. Borras, V. Chiochia, D. Dannheim⁹, G. Drews, J. Fourletova, U. Fricke, A. Geiser, P. Göttlicher¹⁰, O. Gutsche, T. Haas, W. Hain, S. Hillert¹¹, C. Horn, B. Kahle, U. Kötz, H. Kowalski, G. Kramberger, H. Labes, D. Lelas, H. Lim, B. Löhr, R. Mankel, I.-A. Melzer-Pellmann, C.N. Nguyen, D. Notz, A.E. Nuncio-Quiroz, A. Polini, A. Raval, U. Schneekloth, U. Stösslein, G. Wolf, C. Youngman, W. Zeuner
Deutsches Elektronen-Synchrotron DESY, Hamburg, Germany

S. Schlenstedt
DESY Zeuthen, Zeuthen, Germany

G. Barbagli, E. Gallo, C. Genta, P. G. Pelfer
University and INFN, Florence, Italy^e

A. Bamberger, A. Benen, F. Karstens, D. Dobur, N.N. Vlasov¹²
Fakultät für Physik der Universität Freiburg i.Br., Freiburg i.Br., Germany^b

P.J. Bussey, A.T. Doyle, J. Ferrando, J. Hamilton, S. Hanlon, D.H. Saxon, I.O. Skillicorn
Department of Physics and Astronomy, University of Glasgow, Glasgow, United Kingdom^m

I. Gialas
Department of Engineering in Management and Finance, Univ. of Aegean, Greece

T. Carli, T. Gosau, U. Holm, N. Krumnack, E. Lohrmann, M. Milite, H. Salehi, P. Schleper, T. Schörner-Sadenius, S. Stonjek¹¹, K. Wichmann, K. Wick, A. Ziegler, Ar. Ziegler
Hamburg University, Institute of Exp. Physics, Hamburg, Germany^b

C. Collins-Tooth¹³, C. Foudas, R. Gonçalo¹⁴, K.R. Long, A.D. Tapper
Imperial College London, High Energy Nuclear Physics Group, London, United Kingdom^m

P. Cloth, D. Filges
Forschungszentrum Jülich, Institut für Kernphysik, Jülich, Germany

M. Kataoka¹⁵, K. Nagano, K. Tokushuku¹⁶, S. Yamada, Y. Yamazaki
Institute of Particle and Nuclear Studies, KEK, Tsukuba, Japan^f

A.N. Barakbaev, E.G. Boos, N.S. Pokrovskiy, B.O. Zhautykov
Institute of Physics and Technology of Ministry of Education and Science of Kazakhstan, Almaty, Kazakhstan

D. Son
*Kyungpook National University, Center for High Energy Physics, Daegu, South Korea*⁹

J. de Favereau, K. Piotrkowski
Institut de Physique Nucléaire, Université Catholique de Louvain, Louvain-la-Neuve, Belgium

F. Barreiro, C. Glasman¹⁷, O. González, L. Labarga, J. del Peso, E. Tassi, J. Terrón,
M. Zambrana

Departamento de Física Teórica, Universidad Autónoma de Madrid, Madrid, Spain^l

M. Barbi, F. Corriveau, S. Gliga, J. Lainesse, S. Padhi, D.G. Stairs, R. Walsh
Department of Physics, McGill University, Montréal, Québec, Canada H3A 2T8^a

T. Tsurugai

Meiji Gakuin University, Faculty of General Education, Yokohama, Japan^f

A. Antonov, P. Danilov, B.A. Dolgoshein, D. Gladkov, V. Sosnovtsev, S. Suchkov
Moscow Engineering Physics Institute, Moscow, Russia^j

R.K. Dementiev, P.F. Ermolov, I.I. Katkov, L.A. Khein, I.A. Korzhavina, V.A. Kuzmin,
B.B. Levchenko, O.Yu. Lukina, A.S. Proskuryakov, L.M. Shcheglova, S.A. Zotkin
Moscow State University, Institute of Nuclear Physics, Moscow, Russia^k

I. Abt, C. Büttner, A. Caldwell, X. Liu, J. Sutiak

Max-Planck-Institut für Physik, München, Germany

N. Coppola, G. Grigorescu, S. Griepink, A. Keramidas, E. Koffeman, P. Kooijman,
E. Maddox, A. Pellegrino, S. Schagen, H. Tiecke, M. Vázquez, L. Wiggers, E. de Wolf
NIKHEF and University of Amsterdam, Amsterdam, Netherlands^h

N. Brümmer, B. Bylsma, L.S. Durkin, T.Y. Ling

Physics Department, Ohio State University, Columbus, Ohio 43210ⁿ

A.M. Cooper-Sarkar, A. Cottrell, R.C.E. Devenish, B. Foster, G. Grzelak, C. Gwenlan¹⁸,
T. Kohno, S. Patel, P.B. Straub, R. Walczak

Department of Physics, University of Oxford, Oxford United Kingdom^m

P. Bellan, A. Bertolin, R. Brugnera, R. Carlin, F. Dal Corso, S. Dusini, A. Garfagnini,
S. Limentani, A. Longhin, A. Parenti, M. Posocco, L. Stanco, M. Turcato

Dipartimento di Fisica dell'Università and INFN, Padova, Italy^e

E.A. Heaphy, F. Metlica, B.Y. Oh, J.J. Whitmore¹⁹

*Department of Physics, Pennsylvania State University, University Park, Pennsylvania
16802^o*

Y. Iga

Polytechnic University, Sagamihara, Japan^f

G. D'Agostini, G. Marini, A. Nigro

Dipartimento di Fisica, Università 'La Sapienza' and INFN, Rome, Italy^e

C. Cormack²⁰, J.C. Hart, N.A. McCubbin

Rutherford Appleton Laboratory, Chilton, Didcot, Oxon, United Kingdom^m

C. Heusch

University of California, Santa Cruz, California 95064, USA ⁿ

I.H. Park

Department of Physics, Ewha Womans University, Seoul, Korea

H. Abramowicz, A. Gabareen, S. Kananov, A. Kreisel, A. Levy

Raymond and Beverly Sackler Faculty of Exact Sciences, School of Physics, Tel-Aviv University, Tel-Aviv, Israel ^d

M. Kuze

Department of Physics, Tokyo Institute of Technology, Tokyo, Japan ^f

T. Fusayasu, S. Kagawa, T. Tawara, T. Yamashita

Department of Physics, University of Tokyo, Tokyo, Japan ^f

R. Hamatsu, T. Hirose², M. Inuzuka, H. Kaji, S. Kitamura²¹, K. Matsuzawa

Tokyo Metropolitan University, Department of Physics, Tokyo, Japan ^f

M. Costa, M.I. Ferrero, V. Monaco, R. Sacchi, A. Solano

Università di Torino and INFN, Torino, Italy ^e

M. Arneodo, M. Ruspa

Università del Piemonte Orientale, Novara, and INFN, Torino, Italy ^e

T. Koop, J.F. Martin, A. Mirea

Department of Physics, University of Toronto, Toronto, Ontario, Canada M5S 1A7 ^a

J.M. Butterworth²², R. Hall-Wilton, T.W. Jones, M.S. Lightwood, M.R. Sutton⁴, C. Targett-Adams

Physics and Astronomy Department, University College London, London, United Kingdom ^m

J. Ciborowski²³, R. Ciesielski²⁴, P. Łuźniak²⁵, R.J. Nowak, J.M. Pawlak, J. Sztuk²⁶,

T. Tymieniecka, A. Ukleja, J. Ukleja²⁷, A.F. Żarnecki

Warsaw University, Institute of Experimental Physics, Warsaw, Poland ^q

M. Adamus, P. Plucinski

Institute for Nuclear Studies, Warsaw, Poland ^q

Y. Eisenberg, D. Hochman, U. Karshon M. Riveline

Department of Particle Physics, Weizmann Institute, Rehovot, Israel ^c

A. Everett, L.K. Gladilin²⁸, D. Kçira, S. Lammers, L. Li, D.D. Reeder, M. Rosin, P. Ryan, A.A. Savin, W.H. Smith

Department of Physics, University of Wisconsin, Madison, Wisconsin 53706, USA ⁿ

S. Dhawan

Department of Physics, Yale University, New Haven, Connecticut 06520-8121, USA ⁿ

S. Bhadra, C.D. Catterall, S. Furler, G. Hartner, S. Menary, M. Soares, J. Standage

Department of Physics, York University, Ontario, Canada M3J 1P3 ^a

- ¹ also affiliated with University College London, UK
- ² retired
- ³ self-employed
- ⁴ PPARC Advanced fellow
- ⁵ now at Dongshin University, Naju, South Korea
- ⁶ partly supported by Polish Ministry of Scientific Research and Information Technology, grant no. 2P03B 12225
- ⁷ partly supported by Polish Ministry of Scientific Research and Information Technology, grant no.2P03B 12625
- ⁸ supported by the Polish State Committee for Scientific Research, grant no. 2 P03B 09322
- ⁹ now at Columbia University, N.Y., USA
- ¹⁰ now at DESY group FEB
- ¹¹ now at University of Oxford, UK
- ¹² partly supported by Moscow State University, Russia
- ¹³ now at the Department of Physics and Astronomy, University of Glasgow, UK
- ¹⁴ now at Royal Holloway University of London, UK
- ¹⁵ also at Nara Women's University, Nara, Japan
- ¹⁶ also at University of Tokyo, Japan
- ¹⁷ Ramón y Cajal Fellow
- ¹⁸ PPARC Postdoctoral Research Fellow
- ¹⁹ on leave of absence at The National Science Foundation, Arlington, VA, USA
- ²⁰ now at Queen Mary College, University of London, UK
- ²¹ present address: Tokyo Metropolitan University of Health Sciences, Tokyo 116-8551, Japan
- ²² also at University of Hamburg, Alexander von Humboldt Fellow
- ²³ also at Łódź University, Poland
- ²⁴ supported by the Polish State Committee for Scientific Research, grant no. 2P03B 07222
- ²⁵ Łódź University, Poland
- ²⁶ Łódź University, Poland, supported by the KBN grant 2P03B12925
- ²⁷ supported by the KBN grant 2P03B12725
- ²⁸ on leave from Moscow State University, Russia, partly supported by the Weizmann Institute via the U.S.-Israel Binational Science Foundation

- ^a supported by the Natural Sciences and Engineering Research Council of Canada (NSERC)
- ^b supported by the German Federal Ministry for Education and Research (BMBF), under contract numbers HZ1GUA 2, HZ1GUB 0, HZ1PDA 5, HZ1VFA 5
- ^c supported in part by the MINERVA Gesellschaft für Forschung GmbH, the Israel Science Foundation (grant no. 293/02-11.2), the U.S.-Israel Binational Science Foundation and the Benozio Center for High Energy Physics
- ^d supported by the German-Israeli Foundation and the Israel Science Foundation
- ^e supported by the Italian National Institute for Nuclear Physics (INFN)
- ^f supported by the Japanese Ministry of Education, Culture, Sports, Science and Technology (MEXT) and its grants for Scientific Research
- ^g supported by the Korean Ministry of Education and Korea Science and Engineering Foundation
- ^h supported by the Netherlands Foundation for Research on Matter (FOM)
- ⁱ supported by the Polish State Committee for Scientific Research, grant no. 620/E-77/SPB/DESY/P-03/DZ 117/2003-2005
- ^j partially supported by the German Federal Ministry for Education and Research (BMBF)
- ^k supported by RF President grant N 1685.2003.2 for the leading scientific schools and by the Russian Ministry of Industry, Science and Technology through its grant for Scientific Research on High Energy Physics
- ^l supported by the Spanish Ministry of Education and Science through funds provided by CICYT
- ^m supported by the Particle Physics and Astronomy Research Council, UK
- ⁿ supported by the US Department of Energy
- ^o supported by the US National Science Foundation
- ^p supported by the Polish Ministry of Scientific Research and Information Technology, grant no. 112/E-356/SPUB/DESY/P-03/DZ 116/2003-2005
- ^q supported by the Polish State Committee for Scientific Research, grant no. 115/E-343/SPUB-M/DESY/P-03/DZ 121/2001-2002, 2 P03B 07022

1 Introduction

Jet production in ep collisions provides a fruitful testing ground of perturbative QCD (pQCD). Measurements of differential cross sections for jet production [1–9] have allowed detailed studies of parton dynamics, tests of the proton and photon parton distribution functions (PDFs) as well as precise determinations of the strong coupling constant, α_s . Most of these measurements refer to the production of jets irrespective of their partonic origin – quarks or gluons – and, therefore, have only provided general tests of the partonic structure of the short-distance process and of combinations of the proton and/or photon PDFs. The identification of quark- and gluon-initiated jets would allow more stringent tests of the QCD predictions. Such measurements of the production of jets containing a heavy quark have been made by means of tagging specific decay channels [10]. In the present study, quark- and gluon-initiated jets are identified on a statistical basis by utilising their internal structure.

Two kinematic regimes have been studied: photoproduction (γp) and neutral current (NC) deep inelastic ep scattering (DIS). Photoproduction at HERA is studied by means of ep scattering at low four-momentum transfers ($Q^2 \approx 0$, where Q^2 is the virtuality of the exchanged photon). In photoproduction, two types of QCD processes contribute to jet production at leading order (LO) [11, 12]: either the photon interacts directly with a parton in the proton (the direct process) or the photon acts as a source of partons which scatter off those in the proton (the resolved process). Jet production in NC DIS up to LO in α_s proceeds as in the quark-parton model ($Vq \rightarrow q$, where $V = \gamma$ or Z^0) or via the boson-gluon fusion ($Vg \rightarrow q\bar{q}$) and QCD-Compton ($Vq \rightarrow qg$) processes.

This paper is organised as follows. Section 2 gives the theoretical expectations for the measurements presented. The experimental set-up and data selection are described in Sections 3 and 4, respectively. Section 5 explains the QCD calculations used in this analysis. The corrections applied to the data and systematic uncertainties are given in Section 6. The results on the mean integrated jet shape and subjet multiplicity in photoproduction and NC DIS are presented in Section 7. The measurements of differential inclusive jet cross sections as a function of the jet pseudorapidity¹, η^{jet} , and jet transverse energy, E_T^{jet} , for samples of jets in the photoproduction and NC DIS regimes, separated according to their shape and subjet multiplicity, are presented in Section 8. In addition, measurements of differential dijet cross sections in photoproduction as a function of $\cos \theta^*$, where θ^* is the angle between the jet-jet axis and the beam direction in the dijet centre-of-mass system, the dijet invariant mass, M^{jj} , and the fraction of the photon momentum participating in

¹ The ZEUS coordinate system is a right-handed Cartesian system, with the Z axis pointing in the proton beam direction, referred to as the “forward direction”, and the X axis pointing left towards the centre of HERA. The coordinate origin is at the nominal interaction point.

the production of the two jets with highest E_T^{jet} , x_γ^{obs} , are also presented for a variety of tagged-jet configurations. The results are compared to leading-logarithm parton-shower calculations and used to investigate the dynamics underlying the production of specific tagged-jet final states. Finally, in Section 9, the measurements of the mean integrated jet shape in NC DIS are compared to next-to-leading-order (NLO) QCD predictions and used to extract α_s .

2 Theoretical expectations

The internal structure of a jet depends mainly on the type of primary parton – quark or gluon – from which it originated and to a lesser extent on the particular hard scattering process. At sufficiently high jet transverse energy, where the influence of fragmentation effects becomes negligible, the internal structure of a jet is calculable in pQCD. Such calculations predict that gluon-initiated jets are broader than quark-initiated jets due to the larger colour charge of the gluon. The jet shape [13] and subjet multiplicity [14] can be used to study the internal structure of the jets and to classify them: a “broad”-jet sample is enriched in gluon-initiated jets, whereas a “narrow”-jet sample is enriched in quark-initiated jets. Thus, measurements of cross sections for broad- and narrow-jet samples allow the contributing hard-scattering subprocesses to be disentangled.

The dominant partonic subprocesses responsible for jet photoproduction in the kinematic region presented in this paper are $\gamma g \rightarrow q\bar{q}$ and $q_\gamma g_p \rightarrow qg$, where q_γ (g_p) denotes a quark (gluon) coming from the photon (proton). The kinematics of these two-to-two subprocesses are such that the majority of the jets in the region $\eta^{\text{jet}} < 0$ originate from outgoing quarks, whereas the fraction of gluon-initiated jets increases as η^{jet} increases.

The distribution in θ^* reflects the underlying parton dynamics and is sensitive to the spin of the exchanged particle. In the case of direct-photon interactions, the contributing subprocesses at LO QCD are (i) $\gamma q(\bar{q}) \rightarrow qg(\bar{q})$ and (ii) $\gamma g \rightarrow q\bar{q}$, which involve quark exchange. The behaviour of the dijet angular distribution as $|\cos \theta^*| \rightarrow 1$ is the same for all direct subprocesses and proportional to $(1 - |\cos \theta^*|)^{-1}$. In the case of resolved-photon interactions, the contributing subprocesses are $qg \rightarrow qg$, $qq' \rightarrow qq'$, $gg \rightarrow gg$, The dominant subprocesses are those that involve gluon exchange and the behaviour of the dijet angular distribution as $|\cos \theta^*| \rightarrow 1$ is proportional to $(1 - |\cos \theta^*|)^{-2}$. The different behaviour of the dijet angular distribution for resolved and direct processes has been measured in photoproduction at HERA [3, 15]. The study of the angular distribution for dijet events with tagged quark- and/or gluon-initiated jets in the final state, provides then a handle to investigate the underlying parton dynamics further.

Measurements of jet substructure in NC DIS allow a determination of α_s . In zeroth-order

pQCD, a jet consists of only one parton and the jets have no substructure. The first non-trivial contribution to the jet substructure is given by $\mathcal{O}(\alpha_s)$ processes in which, e.g., a quark radiates a gluon at a small angle; these are proportional to the rate of parton emission and thus to α_s . For DIS in the laboratory frame, all necessary QCD corrections to the jet cross sections for the determination of α_s from the jet substructure are available.

2.1 Jet-shape and subjet-multiplicity definitions

The k_T cluster algorithm [16] was used in the longitudinally invariant inclusive mode [17] to define jets in the hadronic final state. The integrated jet shape, $\psi(r)$, is defined using only those particles belonging to the jet as the fraction of the jet transverse energy that lies inside a cone in the $\eta - \varphi$ plane of radius r concentric with the jet axis:

$$\psi(r) = \frac{E_T(r)}{E_T^{\text{jet}}},$$

where $E_T(r)$ is the transverse energy within the given cone of radius r . The mean integrated jet shape, $\langle\psi(r)\rangle$, is defined as the averaged fraction of the jet transverse energy inside the cone r :

$$\langle\psi(r)\rangle = \frac{1}{N_{\text{jets}}} \sum_{\text{jets}} \frac{E_T(r)}{E_T^{\text{jet}}},$$

where N_{jets} is the total number of jets in the sample.

The integrated jet shape is calculated at LO in pQCD as the fraction of the jet transverse energy, due to parton emission, that lies in the cone segment between r and $R = 1$:

$$\langle 1 - \psi(r) \rangle = \frac{\int dE_T (E_T/E_T^{\text{jet}}) [d\sigma(ep \rightarrow 2 \text{ partons})/dE_T]}{\sigma_{\text{jet}}(E_T^{\text{jet}})},$$

where $\sigma_{\text{jet}}(E_T^{\text{jet}})$ is the cross section for inclusive jet production. In the NLO QCD predictions of the integrated jet shape, the numerator in the above formula is calculated to $\mathcal{O}(\alpha_s^2)$ and the denominator to $\mathcal{O}(\alpha_s)$.

Studies of QCD using jet production in NC DIS at HERA are usually performed in the Breit frame. The analysis of jet shapes presented here was performed in the laboratory frame, since calculations of this observable in the Breit frame can, at present, only be performed to $\mathcal{O}(\alpha_s)$, precluding a reliable determination of α_s . However, calculations of the jet shape can be performed up to $\mathcal{O}(\alpha_s^2)$ in the laboratory frame. Furthermore, the analysis was performed in the kinematic region defined by $Q^2 > 125 \text{ GeV}^2$ since, at lower values of Q^2 , the sample of events with at least one jet with $E_T^{\text{jet}} > 17 \text{ GeV}$ is dominated by

dijet events. The calculation of the integrated jet shape for dijet events can be performed only up to $\mathcal{O}(\alpha_s)$, which would severely restrict the accuracy of the predictions.

Subjects were resolved within a jet by considering all particles associated with the jet and repeating the application of the k_T cluster algorithm until, for every pair of particles i and j the quantity $d_{ij} = \min(E_{T,i}, E_{T,j})^2 \cdot ((\eta_i - \eta_j)^2 + (\varphi_i - \varphi_j)^2)$, where $E_{T,i}$, η_i and φ_i are the transverse energy, pseudorapidity and azimuth of particle i , respectively, was greater than $d_{\text{cut}} = y_{\text{cut}}(E_T^{\text{jet}})^2$. All remaining clusters were called subjects. The subject multiplicity, n_{subject} , depends upon the value chosen for the resolution parameter y_{cut} . The mean subject multiplicity, $\langle n_{\text{subject}} \rangle$, is defined as the average number of subjects contained in a jet at a given value of y_{cut} :

$$\langle n_{\text{subject}}(y_{\text{cut}}) \rangle = \frac{1}{N_{\text{jets}}} \sum_{i=1}^{N_{\text{jets}}} n_{\text{subject}}^i(y_{\text{cut}}),$$

where $n_{\text{subject}}^i(y_{\text{cut}})$ is the number of subjects in jet i .

3 Experimental set-up

The data used in this analysis were collected during the 1998-2000 running period, when HERA operated with protons of energy $E_p = 920$ GeV and electrons or positrons² of energy $E_e = 27.5$ GeV, and correspond to an integrated luminosity of 82.2 ± 1.9 pb⁻¹.

A detailed description of the ZEUS detector can be found elsewhere [18,19]. A brief outline of the components that are most relevant for this analysis is given below. Charged particles are tracked in the central tracking detector (CTD) [20], which operates in a magnetic field of 1.43 T provided by a narrow superconducting solenoid. The CTD consists of 72 cylindrical drift-chamber layers, organized in nine superlayers covering the polar-angle region $15^\circ < \theta < 164^\circ$. The transverse-momentum resolution for full-length tracks can be parameterised as $\sigma(p_T)/p_T = 0.0058p_T \oplus 0.0065 \oplus 0.0014/p_T$, with p_T in GeV. The tracking system was used to measure the interaction vertex with a typical resolution along (transverse to) the beam direction of 0.4 (0.1) cm and to cross-check the energy scale of the calorimeter.

The high-resolution uranium–scintillator calorimeter (CAL) [21] covers 99.7% of the total solid angle and consists of three parts: the forward (FCAL), the barrel (BCAL) and the rear (RCAL) calorimeters. Each part is subdivided transversely into towers and longitudinally into one electromagnetic section (EMC) and either one (in RCAL) or two (in

² Here and in the following, the term “electron” denotes generically both the electron (e^-) and the positron (e^+).

BCAL and FCAL) hadronic sections (HAC). The smallest subdivision of the calorimeter is called a cell. Under test-beam conditions, the CAL single-particle relative energy resolutions were $\sigma(E)/E = 0.18/\sqrt{E}$ for electrons and $\sigma(E)/E = 0.35/\sqrt{E}$ for hadrons, with E in GeV.

The luminosity was measured from the rate of the bremsstrahlung process $ep \rightarrow e\gamma p$. The resulting small-angle energetic photons were measured by the luminosity monitor [22], a lead-scintillator calorimeter placed in the HERA tunnel at $Z = -107$ m.

4 Data selection and jet search

A three-level trigger system was used to select events online [19, 23]. At the first level, events were triggered by a coincidence of a regional or transverse energy sum in the CAL and at least one track from the interaction point measured in the CTD. At the second level, a total transverse energy of at least 8 GeV, excluding the energy in the eight CAL towers immediately surrounding the forward beampipe, was required, and cuts on CAL energies and timing were used to suppress events caused by interactions between the proton beam and residual gas in the beampipe. At the third level, a jet algorithm was applied to the CAL cells and jets were reconstructed using the energies and positions of these cells. Events with at least one (two) jet(s) with $E_T > 10$ (6) GeV and $\eta < 2.5$ were accepted for the inclusive jet (dijet) samples. For systematic trigger studies, all events with a total transverse energy of at least 25 GeV, excluding the energy in the eight CAL towers immediately surrounding the forward beampipe, were accepted. No jet algorithm was applied in this case.

In the offline selection, a reconstructed event vertex consistent with the nominal interaction position was required and cuts based on the tracking information were applied to reduce beam-induced interactions and cosmic-ray events. The main steps of the selection of photoproduction and DIS events are briefly explained below.

4.1 Selection of the photoproduction sample

Events from collisions between quasi-real photons and protons were selected offline using similar criteria to those reported in a previous publication [2, 5]. Charged current DIS events were rejected by requiring the total missing transverse momentum, p_T^{miss} , to be small compared to the total transverse energy, E_T^{tot} , $p_T^{\text{miss}}/\sqrt{E_T^{\text{tot}}} < 2\sqrt{\text{GeV}}$. Any NC DIS events with an identified scattered-electron candidate in the CAL [24] were removed from the sample using the method described previously [25]. The remaining background

from NC DIS events was estimated by Monte Carlo (MC) techniques to be below 0.3% and was neglected.

The selected sample consisted of events from ep interactions with $Q^2 \lesssim 1 \text{ GeV}^2$ and a median $Q^2 \approx 10^{-3} \text{ GeV}^2$. The γp centre-of-mass energy is given by $W_{\gamma p} = \sqrt{sy}$, where y is the inelasticity variable and \sqrt{s} is the ep centre-of-mass energy, $s = 4E_e E_p$. The inelasticity variable was reconstructed using the method of Jacquet-Blondel [26], $y_{\text{JB}} = (E - p_Z)/2E_e$, where E is the total CAL energy and p_Z is the Z component of the energy measured in the CAL cells. The value of y was systematically underestimated by $\sim 20\%$ with an r.m.s. of $\sim 10\%$. This effect, which was due to energy lost in the inactive material in front of the CAL and to particles lost in the rear beampipe, was satisfactorily reproduced by the MC simulation of the detector. The MC event samples were therefore used to correct for this underestimation. The photoproduction sample was restricted to $142 < W_{\gamma p} < 293 \text{ GeV}$ [2, 5].

4.2 Selection of the NC DIS sample

Events from NC DIS interactions were selected offline using similar criteria to those reported in a previous publication [27]. The scattered-electron candidate was identified using the pattern of energy deposits in the CAL [24]. The energy, E'_e , and polar angle, θ_e , of the electron candidate were also determined from the CAL measurements. The double-angle method [28], which uses θ_e and an angle γ that corresponds, in the quark-parton model, to the direction of the scattered quark, was used to reconstruct Q^2 , Q_{DA}^2 . The angle γ was reconstructed using the CAL measurements of the hadronic final state.

An electron candidate of energy $E'_e > 10 \text{ GeV}$ was required to ensure a high and well understood electron-finding efficiency and to suppress background from photoproduction. The inelasticity variable as reconstructed from the electron, y_e , was required to be below 0.95. This condition removed events in which fake electron candidates from photoproduction background were found in the FCAL. The requirements $38 < (E - p_Z) < 65 \text{ GeV}$, to remove events with large initial-state radiation and to reduce further the photoproduction background, and $p_T^{\text{miss}}/\sqrt{E_T^{\text{tot}}} < 3 \sqrt{\text{GeV}}$, to remove cosmic rays and beam-related background, were applied. The kinematic range was restricted to $Q_{\text{DA}}^2 > 125 \text{ GeV}^2$.

4.3 Jet search

The k_T cluster algorithm was used in the longitudinally invariant inclusive mode to reconstruct jets in the hadronic final state from the energy deposits in the CAL cells. For DIS events, the jet algorithm was applied after excluding those cells associated with the

scattered-electron candidate. The jet search was performed in the $\eta - \varphi$ plane of the laboratory frame. The jet variables were defined according to the Snowmass convention [29]. The jets reconstructed from the CAL cell energies are called calorimetric jets and the variables associated with them are denoted by $E_{T,\text{cal}}^{\text{jet}}$, $\eta_{\text{cal}}^{\text{jet}}$ and $\varphi_{\text{cal}}^{\text{jet}}$. A total of 199 237 (98 240) events with at least one jet satisfying $E_{T,\text{cal}}^{\text{jet}} > 13$ GeV and $-1 < \eta_{\text{cal}}^{\text{jet}} < 2.5$ were selected in the photoproduction (DIS) sample.

5 QCD calculations

5.1 Leading-logarithm parton-shower Monte Carlo models

The programs PYTHIA 6.1 [30] and HERWIG 6.1 [31] were used to generate photoproduction events for resolved and direct processes. Events were generated using GRV-HO [32] for the photon and CTEQ4M [33] for the proton PDFs. In both generators, the partonic processes are simulated using LO matrix elements, with the inclusion of initial- and final-state parton showers. Fragmentation into hadrons is performed using the Lund string model [34] as implemented in JETSET [30,35] in the case of PYTHIA, and a cluster model [36] in the case of HERWIG. Samples of PYTHIA including multiparton interactions (MI) [37] with a minimum transverse momentum for the secondary scatter of 1 GeV [38] were used to study the effects of a possible “underlying event”.

Neutral current DIS events including radiative effects were simulated using the HERACLES 4.6.1 [39] program with the DJANGO 1.1 [40] interface to the hadronisation programs. HERACLES includes corrections for initial- and final-state radiation, vertex and propagator terms, and two-boson exchange. The QCD cascade is simulated using the colour-dipole model (CDM) [41] including the LO QCD diagrams as implemented in ARIADNE 4.08 [42] and, as a systematic check of the final results, with the MEPS model of LEPTO 6.5 [43]. Both MC programs use the Lund string model for the hadronisation. The CTEQ5D [44] proton PDFs were used for these simulations.

These MC samples were used to correct the data to the hadron level, defined as those hadrons with lifetime $\tau \geq 10$ ps. For this purpose, the generated events were passed through the ZEUS detector- and trigger-simulation programs based on GEANT 3.13 [45]. They were reconstructed and analysed by the same program chain as the data. The jet search was performed using the energy measured in the CAL cells in the same way as for the data. The same jet algorithm was also applied to the final-state particles and to the partons available after the parton shower; the jets found in this way are referred to as hadronic and partonic jets, respectively.

Electroweak-radiative, hadronisation and Z^0 -exchange effects are not at present included

in the NLO QCD programs described in Section 5.2. Therefore, samples of MC events were generated without electroweak-radiative effects so that the data could be corrected for these effects when comparing with the NLO QCD predictions. Additional samples of MC events without Z^0 -exchange effects were generated to correct the NLO QCD calculations for these effects and for hadronisation.

5.2 NLO QCD calculations

The NLO QCD calculations of the mean integrated jet shapes in DIS³ are based on the program DISENT [46]. The calculations use a generalised version of the subtraction method [47] and are performed in the massless $\overline{\text{MS}}$ renormalisation and factorisation schemes. The number of flavours was set to five; the renormalisation (μ_R) and factorisation (μ_F) scales were both set to $\mu_R = \mu_F = Q$; α_s was calculated at two loops using $\Lambda_{\overline{\text{MS}}}^{(5)} = 220$ MeV, which corresponds to $\alpha_s(M_Z) = 0.1175$. The MRST99 [48] parameterisations of the proton PDFs were used as defaults for the comparisons with the data. The calculations obtained with DISENT were cross-checked by using the program DISASTER++ [49]. The differences were smaller than 0.5% for $r \geq 0.3$.

Since the measurements refer to jets of hadrons, whereas the QCD calculations refer to partons, the predictions were corrected to the hadron level using the MC samples described in Section 5.1. The multiplicative correction factor, C_{had} , defined as $\langle\psi(r)\rangle_{\text{had}}/\langle\psi(r)\rangle_{\text{par}}$, where $\langle\psi(r)\rangle_{\text{par}}$ ($_{\text{had}}$) is the mean integrated jet shape before (after) the hadronisation process, was estimated with both the CDM and MEPS models. The procedure for applying hadronisation corrections to the NLO QCD calculations was verified by checking that the MC predictions for the integrated jet shape at the parton level reproduced the NLO QCD calculations. The agreement was well within 0.2% after adjusting the contributions of the different subprocesses ($eq \rightarrow eq$, $eg \rightarrow eq\bar{q}$ and $eq \rightarrow eqg$) in the MC to reproduce the η^{jet} cross section and jet shape of the NLO calculations. The values of C_{had} obtained with the CDM model were taken as the defaults; the predictions from the two models were in good agreement. The value of C_{had} was 0.95 at $r = 0.5$ for $E_T^{\text{jet}} = 21$ GeV and approached unity as E_T^{jet} increased.

³ Only QCD calculations of jet shapes in DIS are compared to the data because there is no NLO program available for similar calculations in photoproduction.

6 Corrections and systematic uncertainties

6.1 Jet energy corrections

The comparison of the reconstructed jet variables for the hadronic and the calorimetric jets in simulated events showed that no correction was needed for η^{jet} and φ^{jet} ($\eta^{\text{jet}} \simeq \eta_{\text{cal}}^{\text{jet}}$ and $\varphi^{\text{jet}} \simeq \varphi_{\text{cal}}^{\text{jet}}$). However, the transverse energy of the calorimetric jet was an underestimate of the corresponding hadronic jet energy by an average of $\sim 15\%$, with an r.m.s. of $\sim 10\%$. This underestimation was mainly due to the energy lost by the particles in the inactive material in front of the CAL. The transverse-energy corrections to calorimetric jets, as a function of $\eta_{\text{cal}}^{\text{jet}}$ and $E_{T,\text{cal}}^{\text{jet}}$ and averaged over $\varphi_{\text{cal}}^{\text{jet}}$, were determined for the photoproduction and DIS samples using the corresponding MC-generated events [2, 3, 27]. Henceforth, jet variables without subscript refer to the corrected values. After these corrections to the jet transverse energy, events with at least one jet satisfying $E_T^{\text{jet}} > 17$ GeV and $-1 < \eta^{\text{jet}} < 2.5$ were retained for the studies of inclusive jet observables and events with at least two jets with $E_T^{\text{jet}1} > 17$ GeV, $E_T^{\text{jet}2} > 14$ GeV and $-1 < \eta^{\text{jet}} < 2.5$, where the jets are labelled in decreasing E_T^{jet} order, were retained for the dijet studies.

6.2 Acceptance corrections

Using the selected data sample of inclusive jets with $E_T^{\text{jet}} > 17$ GeV and $-1 < \eta^{\text{jet}} < 2.5$, in the kinematic region defined by $Q^2 < 1$ GeV² and $142 < W_{\gamma p} < 293$ GeV in photoproduction and $Q^2 > 125$ GeV² in DIS, the mean integrated jet shape and mean subjet multiplicity were reconstructed using the CAL cells and corrected to the hadron level by MC techniques. The corrected values were determined bin-by-bin using the MC samples separately for each region of η^{jet} and E_T^{jet} studied. For this approach to be valid, the distributions of the uncorrected integrated jet shape and subjet multiplicity in the data must be well described by the MC simulations at the detector level. This condition was in general satisfied by the MC photoproduction models. In DIS, to obtain the best description of the uncorrected jet shape in the data by the MC simulations, the contributions of the different subprocesses ($eq \rightarrow eq$, $eg \rightarrow eq\bar{q}$ and $eq \rightarrow eqg$) were reweighted so as to reproduce the mean integrated jet shape and η^{jet} distributions in the data. This procedure was applied to the simulations of CDM and MEPS and for each region in η^{jet} and E_T^{jet} . The correction factors were evaluated using these tuned versions of CDM and MEPS in DIS and the default mixture of resolved and direct processes in PYTHIA, HERWIG and PYTHIA MI.

Differential jet cross sections were measured using the selected data sample of inclusive jet events. Dijet differential cross sections in photoproduction were measured in the same

kinematic region as above and refer to the two highest- E_T^{jet} jets of hadrons in the event with $E_T^{\text{jet}1} > 17$ GeV, $E_T^{\text{jet}2} > 14$ GeV and $-1 < \eta^{\text{jet}} < 2.5$. The PYTHIA (CDM) MC samples of photoproduction (DIS) events were used to compute the acceptance corrections to the jet distributions. These correction factors took into account the efficiency of the trigger, the selection criteria and the purity and efficiency of the jet reconstruction. The inclusive jet cross sections were obtained by applying bin-by-bin corrections to the measured distributions. The samples of HERWIG and MEPS were used to compute the systematic uncertainties coming from the fragmentation and parton-shower models in photoproduction and DIS, respectively (see Section 6.3).

6.3 Systematic uncertainties

A study of the main sources contributing to the systematic uncertainties of the measurements was performed. The sources considered in the photoproduction measurements are:

- the effect of the treatment of the parton shower and hadronisation was estimated by using the HERWIG generator to evaluate the correction factors;
- the effect of the simulation of the trigger was evaluated by using an alternative trigger configuration, as explained in Section 4, in both data and MC events;
- the effect of the uncertainty on $W_{\gamma p}$ was estimated by varying y_{JB} by its uncertainty of $\pm 1\%$ in simulated events;
- the effect of the uncertainty on the parameterisations of the proton and photon PDFs was estimated by using alternative sets of PDFs in the MC simulation to calculate the correction factors;
- the effect of the uncertainty on the absolute energy scale of the calorimetric jets was estimated by varying E_T^{jet} by its uncertainty of $\pm 1\%$ in simulated events. The method used was the same as in earlier publications [2, 3, 50] and verified with the 98-00 data sample [5].

In the DIS regime, the main sources contributing to the systematic uncertainties of the measurements are:

- the effect of the treatment of the parton shower was estimated by using the MEPS model to evaluate the correction factors;
- the effect of the simulation of the trigger was evaluated by using an alternative trigger configuration, as explained in Section 4, in both data and MC events;

- the effect of the uncertainty on the scattered-electron identification was estimated by using an alternative technique [51] to select the candidates, in both data and MC events;
- the effect of the uncertainty of $\pm 1\%$ in the absolute energy scale of the jets was applied to the simulated events;
- the effect of the uncertainty of $\pm 1\%$ in the absolute energy scale of the scattered-electron candidate was applied to the simulated events.

These uncertainties, for each regime, were added in quadrature to the statistical uncertainty of the data and are shown as error bars in the figures showing the substructure measurements. For the cross-section measurements, the uncertainty arising from that on the absolute energy scale of the jets is shown separately. The uncertainty in the luminosity determination of 2.25% was not included.

7 Measurements of jet substructure

7.1 Jet-shape measurements

The measured mean integrated jet shape as a function of r , $\langle\psi(r)\rangle$, for different regions in η^{jet} is shown in Fig. 1 and Table 1 for the photoproduction regime. The jets broaden as η^{jet} increases. Leading-logarithm parton-shower predictions from PYTHIA for resolved plus direct processes and gluon- and quark-initiated jets are compared to the data in Fig. 1. The measured $\langle\psi(r)\rangle$ is reasonably well described by the MC calculations of PYTHIA for resolved and direct processes for $-1 < \eta^{\text{jet}} < 1.5$, whereas for $1.5 < \eta^{\text{jet}} < 2.5$, the measured jets are slightly broader than the predictions. From the comparison with the predictions for gluon- and quark-initiated jets, it is seen that the measured jets are quark-like for $-1 < \eta^{\text{jet}} < 0$ and become increasingly more gluon-like as η^{jet} increases.

Figure 2 shows the same measurements as Fig. 1, compared to the predictions of PYTHIA including MI. This model gives rise to jets that are much broader than those observed. The predictions using HERWIG, also shown in Fig. 2, describe the data well for $-1 < \eta^{\text{jet}} < 1$, are slightly narrower than the data for $1 < \eta^{\text{jet}} < 1.5$ and fail to describe the data for $1.5 < \eta^{\text{jet}} < 2.5$. These results and those presented below are consistent with the previous ZEUS study of jet shapes in photoproduction [38] which was performed using an iterative cone algorithm and at lower E_T^{jet} .

Figure 3 and Tables 2 and 3 show the $\langle\psi(r)\rangle$ in different regions of E_T^{jet} for the photoproduction regime. The jets become narrower as E_T^{jet} increases. The predictions of PYTHIA for resolved plus direct processes reproduce the data reasonably well. For $17 < E_T^{\text{jet}} < 29$

GeV, the predictions for resolved processes alone also describe the data, consistent with the dominance of resolved processes in this E_T^{jet} region.

Figure 4a shows the measured mean integrated jet shape at a fixed value of $r = 0.5$, $\langle\psi(r = 0.5)\rangle$, as a function of η^{jet} in photoproduction. The predictions of PYTHIA for quark-initiated jets lie above the data, while those for gluon-initiated jets lie below the data. The prediction of PYTHIA, including resolved and direct processes, also shown in Fig. 4a, fails to describe the relatively strong broadening of the measured jet shape for $\eta^{\text{jet}} > 1.5$. This might be because the fraction of gluon-initiated jets in the region $\eta^{\text{jet}} > 1.5$ is underestimated or that the effects of a possible underlying event in the data have not been properly taken into account [38]; however, the prediction of PYTHIA MI fails to describe the data over the whole η^{jet} range. Since $\langle\psi(r = 0.5)\rangle$ changes from a value close to the upper curve (quark-initiated jets) to a value near the lower curve (gluon-initiated jets) as η^{jet} increases, the broadening of $\langle\psi(r = 0.5)\rangle$ as η^{jet} increases is consistent with an increase of the fraction of gluon-initiated jets. The $\langle\psi(r = 0.5)\rangle$ shows an increase with E_T^{jet} (see Fig. 4b). The predictions of PYTHIA for the dependence of $\langle\psi(r = 0.5)\rangle$ on E_T^{jet} in resolved plus direct processes reproduce the data well for $E_T^{\text{jet}} > 21$ GeV. Therefore, the discrepancies between data and MC are concentrated at low E_T^{jet} and high η^{jet} values.

The measured $\langle\psi(r)\rangle$ for different regions of η^{jet} and E_T^{jet} is shown in Figs. 5 and 6 and Tables 4 to 6 for DIS events. Figure 7 shows the measured $\langle\psi(r = 0.5)\rangle$ as a function of η^{jet} and E_T^{jet} . There is no significant variation of $\langle\psi(r = 0.5)\rangle$ with η^{jet} in DIS, whereas $\langle\psi(r = 0.5)\rangle$ increases as E_T^{jet} increases, as observed in a previous study [52] using an iterative cone algorithm. These conclusions are also in agreement with those of a previous publication [27], in which the internal structure of jets in NC DIS was studied using the mean subjet multiplicity.

The NLO QCD calculations of $\langle\psi(r)\rangle$, corrected for hadronisation and Z^0 -exchange effects, are compared to the data in Figs. 5 to 7. The NLO QCD calculations give a good description of $\langle\psi(r)\rangle$ for $r \geq 0.2$; the fractional differences between the measurements and the predictions, also shown in Figs. 5 and 6, are less than 0.2% for $r = 0.5$. The sensitivity of the measurements to the value of $\alpha_s(M_Z)$ is illustrated in Fig. 7b by comparing the measured $\langle\psi(r = 0.5)\rangle$ to NLO QCD calculations using three different values of $\alpha_s(M_Z)$. The NLO QCD calculations provide a good description of the measured $\langle\psi(r = 0.5)\rangle$ and thus this observable was used to determine $\alpha_s(M_Z)$, as explained in Section 9.

Figure 8 shows the η^{jet} and E_T^{jet} dependence of $\langle\psi(r = 0.5)\rangle$ for photoproduction and DIS events; the MC predictions of CDM and PYTHIA for quark- and gluon-initiated jets are compared to the data. Figure 8a shows that the sample of jets in DIS is consistent with being dominated by quark-initiated jets with an approximately constant fraction over the η^{jet} region measured. Photoproduced jets in the backward region are similar to jets in DIS and this agreement confirms, independently of the comparison to MC predictions, that

they are dominated by quark-initiated jets. The increasing deviation in the integrated jet shape for photoproduced jets from that of jets in DIS as η^{jet} (E_T^{jet}) increases (decreases) can be attributed to the increasing fraction of gluon-initiated jets arising from resolved processes.

7.2 Subjet-multiplicity measurements

The measured mean subjet multiplicity as a function of y_{cut} for different regions of η^{jet} and E_T^{jet} for photoproduction is shown in Figs. 9 and 10 and Tables 7 to 9. Figure 11 shows the measured mean subjet multiplicity at a fixed value of $y_{\text{cut}} = 10^{-2}$, $\langle n_{\text{subjet}}(y_{\text{cut}} = 10^{-2}) \rangle$, as a function of η^{jet} and E_T^{jet} . The measured mean subjet multiplicity increases as η^{jet} increases and decreases as E_T^{jet} increases.

The predictions of PYTHIA for quark-initiated, gluon-initiated and all jets at the hadron level are compared to the measurements in Figs. 9 to 11. The predicted $\langle n_{\text{subjet}}(y_{\text{cut}}) \rangle$ is larger for gluon-initiated jets than for quark-initiated jets in each region of η^{jet} . For quark- or gluon-initiated jets alone, $\langle n_{\text{subjet}}(y_{\text{cut}} = 10^{-2}) \rangle$ exhibits only a small dependence on η^{jet} (see Fig. 11a). The η^{jet} -dependence of $\langle n_{\text{subjet}}(y_{\text{cut}} = 10^{-2}) \rangle$ in the calculation for all jets is dictated by the η^{jet} variation of the fractions of quark- and gluon-initiated jets. This variation, in turn, originates from the different dominant two-body subprocess. The calculations using PYTHIA based on the predicted admixture of quark- and gluon-initiated jets give a good description of the measured $\langle n_{\text{subjet}}(y_{\text{cut}}) \rangle$ as a function of y_{cut} , η^{jet} and E_T^{jet} . These results are in agreement with those from the mean integrated jet shape (see Section 7.1).

8 Study of quark and gluon dynamics

The predictions of the MC for the jet shape and subjet multiplicity generally reproduce the data well and show the expected differences for quark- and gluon-initiated jets. These differences are used now to select samples enriched in quark- and gluon-initiated jets to study the dynamics of the hard subprocesses in more detail.

8.1 Selection of quark- and gluon-initiated jets

Quark- and gluon-initiated jets were selected on a statistical basis based on their substructure. The integrated jet shape at $r = 0.3$, $\psi(r = 0.3)$, and the subjet multiplicity at $y_{\text{cut}} = 5 \cdot 10^{-4}$, $n_{\text{subjet}}(y_{\text{cut}} = 5 \cdot 10^{-4})$, were used to select quark- and gluon-initiated jets in the photoproduction and DIS samples. The values $r = 0.3$ and $y_{\text{cut}} = 5 \cdot 10^{-4}$

were chosen to be as small as possible to be sensitive to the differences between quark and gluons, but large enough to avoid uncertainties due to the detector resolution. The different behaviour of these distributions for gluon- and quark-initiated jets is shown in Fig. 12 for samples of PYTHIA and HERWIG generated events. These observables were used to classify the jets into:

- a gluon-enriched sample (broad jets), defined as those jets with $\psi(r = 0.3) < 0.6$ and/or $n_{\text{subjet}}(y_{\text{cut}} = 5 \cdot 10^{-4}) \geq 6$, and
- a quark-enriched sample (narrow jets), defined as those jets with $\psi(r = 0.3) > 0.8$ and/or $n_{\text{subjet}}(y_{\text{cut}} = 5 \cdot 10^{-4}) < 4$.

Non-overlapping ranges were chosen to suppress migration effects. The values for the cuts in $\psi(r = 0.3)$ and $n_{\text{subjet}}(y_{\text{cut}} = 5 \cdot 10^{-4})$ chosen were a compromise between purity and statistics. The purity of the gluon-initiated sample is around 50%, whereas for the quark-enriched sample it is around 90%. Table 10 shows the purities and efficiencies for the different MC and selected samples.

The remaining number of jets after applying the jet-shape, subjet-multiplicity and the combination of both selection cuts in the broad and narrow inclusive jet photoproduction data sample and in the broad-broad, narrow-narrow and broad-narrow dijet data samples selected using the jet-shape method are shown in Table 11. The same table shows also the number of jets in the broad and narrow inclusive jet NC DIS data sample selected according to the jet shape. In the next sections, measurements of cross sections are presented for samples of jets separated according to their shape and/or subjet multiplicity.

8.2 Measurements of $d\sigma/d\eta^{\text{jet}}$

The differential inclusive-jet cross-section $d\sigma/d\eta^{\text{jet}}$ for photoproduction is shown in Fig. 13a and Table 12 for samples of broad and narrow jets, separated according to the jet-shape selection. The measured cross sections exhibit different behaviours: the η^{jet} distribution for broad jets increases up to the highest η^{jet} value measured, whereas the distribution for narrow jets peaks at $\eta^{\text{jet}} \approx 0.7$. Measurements of $d\sigma/d\eta^{\text{jet}}$ in photoproduction for samples of broad and narrow jets separated according to either the subjet-multiplicity selection or a combination of jet shape and subjet multiplicity are shown in Figs. 13c and 13d and Tables 13 and 14, respectively. These measurements also exhibit a difference in shape for the samples of broad and narrow jets. The same conclusions as in the case of using the integrated-jet-shape selection method can be drawn.

Leading-logarithm parton-shower MC calculations using PYTHIA, HERWIG and PYTHIA MI for resolved plus direct photon processes are compared to the measurements in Figs. 13a and 13b. The same selection method was applied to the jets of hadrons in the MC event

samples and the calculations have been normalised to the total measured cross section of each sample. The MC predictions provide a good description of the shape of the narrow-jet distribution in the data. The shape of the broad-jet distribution in the data is reasonably well described by PYTHIA or PYTHIA MI, but the prediction of HERWIG fails to describe this distribution. From the calculation of PYTHIA (HERWIG), the sample of broad jets selected according to the jet shape is predicted to contain 15(12)% of gg subprocesses in the final state and 50(47)% of gq , and a contamination from processes with only quarks in the final state of 35(41)%. There is a large contribution from gq final states in the broad-jet sample because the partonic cross section for the resolved subprocess $q_\gamma g_p \rightarrow gq$ is much larger than the cross section for the subprocesses $q\bar{q} \rightarrow gg$ plus $gg \rightarrow gg$. The sample of narrow jets contains 62(61)% of qq subprocesses and 34(36)% of gq , with a contamination of 4(3)% from gg subprocesses. The measured cross section for the broad-jet sample is $(32.1 \pm 0.1)\%$ of the total cross section, whereas the narrow-jet sample is $(40.6 \pm 0.1)\%$ using the jet-shape selection. PYTHIA (HERWIG) predicts 31.5(27.1)% for the broad-jet sample and 37.4(44.0)% for the narrow-jet sample. Similar conclusions can be drawn from the subjet-multiplicity selection and the combined jet-shape and subjet-multiplicity selection.

Figure 13a also shows the predictions of PYTHIA for jets of quarks and gluons separately. These predictions have been obtained without any jet-shape selection and are normalised to the data cross sections. The calculation that includes only quark-initiated jets gives a good description of the narrow-jet cross section, whereas the calculation for gluon-initiated jets provides a reasonable description of the broad-jet cross section. This result supports the expectation that the broad (narrow)-jet sample is dominated by gluon (quark)-initiated jets.

Figure 14a and Table 15 show $d\sigma/d\eta^{\text{jet}}$ in DIS for samples of broad and narrow jets separated according to the jet shape. The two cross sections have the same variation with η^{jet} , as can be seen from the ratio of the narrow- to the broad-jet cross sections. However, the narrow-jet cross section is about five times larger than the broad-jet cross section, which shows that the DIS sample is enriched in quark-initiated jets. Since the ratio of the cross sections is approximately constant, the quark and gluon content of the final state in DIS does not change with η^{jet} , as also was concluded from Fig. 7a. The predictions of the CDM model are compared to the data in Fig. 14a and give a good description of the data. The predictions of MEPS give a poorer description. Figure 14b shows the same measured cross sections together with the calculations of CDM for gluon- and quark-initiated jets; no jet-shape selection has been applied in this case. These predictions describe well the shapes of the broad- and narrow-jet samples, respectively.

8.3 Measurements of $d\sigma/dE_T^{\text{jet}}$

The differential inclusive jet cross-section $d\sigma/dE_T^{\text{jet}}$, measured in the range $17 < E_T^{\text{jet}} < 95$ GeV, is presented in Figs. 15a and 15b and Tables 16 and 17 for samples of broad and narrow jets, separated according to the jet shape, for photoproduction and DIS events, respectively. The cross sections for the narrow-jet samples have a harder spectrum than that for the broad-jet sample. Figures 15c and 15d and Tables 18 and 19 show the $d\sigma/dE_T^{\text{jet}}$ cross section for samples of broad and narrow jets separated according to the subjet-multiplicity selection and the combined integrated-jet-shape and subjet-multiplicity selection in the photoproduction regime. These measurements exhibit the same behaviour as in Fig. 15a, but the cross-over between the broad- and narrow-jet distributions takes place at slightly higher E_T^{jet} . The MC calculations using PYTHIA, which have been obtained using the same selection method as for the data, are compared to the measurements in Figs. 15a, c and d. The MC predictions provide a good description of the shapes of the data distributions. The predictions of the CDM MC are compared to the measurements in Fig. 15b and give a good description of the data. In photoproduction, the different E_T^{jet} spectra exhibited by the narrow- and broad-jet samples are understood in terms of the increasing fraction of gluon-initiated jets as E_T^{jet} decreases.

8.4 Measurements of $d\sigma/d \cos \theta^*$

For samples of broad-broad or narrow-narrow dijet events, only the absolute value of $\cos \theta^*$ can be determined because the outgoing jets are indistinguishable. The differential dijet cross section as a function of $|\cos \theta^*|$ has been measured in the range $|\cos \theta^*| < 0.8$ for dijet invariant masses $M^{\text{jj}} > 52$ GeV for photoproduction. The region of phase space in the $(M^{\text{jj}}, |\cos \theta^*|)$ plane was chosen in order to minimise the bias introduced by selecting jets with $E_T^{\text{jet}1} > 17$ GeV and $E_T^{\text{jet}2} > 14$ GeV. The measured $d\sigma/d|\cos \theta^*|$ for the samples of broad-broad dijet events and narrow-narrow dijet events are presented in Fig. 16a and Table 20. The measured and predicted cross sections were normalised to unity at $|\cos \theta^*| = 0.1$. The $|\cos \theta^*|$ distribution for the two samples of dijet events increases as $|\cos \theta^*|$ increases; however they exhibit a different slope. The cross section at $|\cos \theta^*| = 0.7$ for broad-broad dijet events is more than seven times larger than the measured value at $|\cos \theta^*| = 0.1$, whereas for narrow-narrow dijet events, the cross section at $|\cos \theta^*| = 0.7$ is only twice as large as at $|\cos \theta^*| = 0.1$.

Calculations using PYTHIA for broad-broad and narrow-narrow dijet events are compared to the data in Fig. 16a. The predictions from PYTHIA give a good description of the shape of the measured $d\sigma/d|\cos \theta^*|$. PYTHIA predicts 16% of gg -final-state subprocesses, 52% of gq and 32% of qq for the broad-broad dijet sample in the kinematic region of this measure-

ment. For the narrow-narrow dijet sample, the predictions are: 71% of qq subprocesses, 28% of qg and 1% of gg . The differences observed in the measured $d\sigma/d|\cos\theta^*|$ for the two samples are adequately reproduced by the calculations and understood in terms of the dominant two-body processes: the resolved subprocess $q_\gamma g_p \rightarrow qq$, mediated by gluon exchange for the broad-broad dijet sample and the direct subprocess $\gamma g \rightarrow q\bar{q}$, mediated by quark exchange for the narrow-narrow dijet sample.

The sample of photoproduced dijet events with one broad jet and one narrow jet allows a measurement of the unfolded $d\sigma/d\cos\theta_{\text{broad}}^*$ cross section. Since in this case the two jets can be distinguished, θ_{broad}^* refers to the scattering angle measured with respect to the broad jet. Figure 16b and Table 21 show the measured dijet cross section as a function of $\cos\theta_{\text{broad}}^*$. The measured and predicted cross sections were normalised to unity at $\cos\theta_{\text{broad}}^* = 0.1$. The dijet angular distribution shows a different behaviour on the negative and positive sides; the measured cross section at $\cos\theta_{\text{broad}}^* = 0.7$ is approximately twice as large as at $\cos\theta_{\text{broad}}^* = -0.7$. The calculation from PYTHIA gives a good description of the shape of the measured $d\sigma/d\cos\theta_{\text{broad}}^*$. The predictions of PYTHIA for the partonic content are: 52% of qg subprocesses, 4% of gg and 44% of qq . The observed asymmetry is adequately reproduced by the calculation and is understood in terms of the dominant resolved subprocess $q_\gamma g_p \rightarrow qq$. The $\cos\theta_{\text{broad}}^*$ distribution for this subprocess is asymmetric due to the different dominant diagrams in the regions $\cos\theta_{\text{broad}}^* \rightarrow \pm 1$: t -channel gluon exchange ($\cos\theta_{\text{broad}}^* \rightarrow +1$) and u -channel quark exchange ($\cos\theta_{\text{broad}}^* \rightarrow -1$).

8.5 Measurements of $d\sigma/dM^{\text{jj}}$ and $d\sigma/dx_\gamma^{\text{obs}}$

The photoproduction differential dijet cross section as a function of M^{jj} has been measured in the range $52 < M^{\text{jj}} < 123$ GeV for $|\cos\theta^*| < 0.8$. The measured $d\sigma/dM^{\text{jj}}$ for the samples of broad-broad and narrow-narrow dijet events are presented in Fig. 16c and Table 22. The measured $d\sigma/dM^{\text{jj}}$ cross sections decrease as M^{jj} increases, but the distribution for the narrow-narrow dijet sample exhibits a harder spectrum, as was also seen for the inclusive jet cross section as a function of E_T^{jet} . The MC calculations from PYTHIA are compared to the data in Fig. 16c and give a good description of the shape of the measured $d\sigma/dM^{\text{jj}}$. The different shape in both cross sections is understood in terms of the dominant two-body processes: the broad-broad dijet sample is dominated by the resolved subprocess $q_\gamma g_p \rightarrow qq$ and the narrow-narrow dijet sample is dominated by the direct subprocess $\gamma g \rightarrow q\bar{q}$. Direct processes reach larger values of M^{jj} than those of resolved since the full incoming-photon energy is available at the hard interaction.

Resolved and direct processes can be separated by using the x_γ^{obs} variable, which is defined as

$$x_\gamma^{\text{obs}} = \frac{1}{2yE_e} (E_T^{\text{jet1}} e^{-\eta^{\text{jet1}}} + E_T^{\text{jet2}} e^{-\eta^{\text{jet2}}}).$$

Resolved and direct processes populate different regions in x_γ^{obs} , with the direct processes concentrated at high values. The dijet cross section as a function of x_γ^{obs} is presented in Fig. 16d and Table 23 and is reasonably well described by the MC predictions of PYTHIA. The cross section for the broad-broad dijet sample is approximately constant as a function of x_γ^{obs} whereas the cross section for the narrow-narrow dijet sample peaks at high values. The shape of the distribution for the broad-broad (narrow-narrow) dijet events is consistent with the dominance of resolved (direct) processes.

9 Determination of α_s

The measured $\langle\psi(r = 0.5)\rangle$ for $E_T^{\text{jet}} > 21$ GeV in DIS was used to determine $\alpha_s(M_Z)$ using a method similar to one presented previously [27]. The NLO QCD calculations were performed using the program DISENT with three different MRST99 sets of proton PDFs, central, MRST99 $\downarrow\downarrow$ and MRST99 $\uparrow\uparrow$; the value of $\alpha_s(M_Z)$ used in each partonic cross-section calculation was that associated with the corresponding set of PDFs. The $\alpha_s(M_Z)$ dependence of the predicted $\langle\psi(r = 0.5)\rangle$ in each bin i of E_T^{jet} was parameterised according to

$$[\langle\psi(r = 0.5)\rangle(\alpha_s(M_Z))]_i = C_1^i + C_2^i\alpha_s(M_Z),$$

where C_1^i and C_2^i were determined from a χ^2 fit by using the NLO QCD calculations corrected for hadronisation and Z^0 -exchange effects. Finally, a value of $\alpha_s(M_Z)$ was determined in each E_T^{jet} region as well as from all the data points by a χ^2 fit.

The values of $\alpha_s(M_Z)$ as determined from the measured $\langle\psi(r = 0.5)\rangle$ in each region of E_T^{jet} are shown in Fig. 17 and Table 24. Taking into account only the statistical uncertainties, the value of $\alpha_s(M_Z)$ obtained by combining all the E_T^{jet} regions is $\alpha_s(M_Z) = 0.1176 \pm 0.0009$ (stat.).

The uncertainties on the extracted value of $\alpha_s(M_Z)$ due to the experimental systematic uncertainties were evaluated by repeating the analysis above for each systematic check described in Section 6.3. The total experimental systematic uncertainty on the value of $\alpha_s(M_Z)$ is $\Delta\alpha_s(M_Z)/\alpha_s(M_Z) = {}^{+0.80}_{-2.2}\%$. The main contribution to the positive (negative) systematic uncertainty comes from the uncertainty in the jet energy scale (scattered-electron identification).

The following sources of theoretical uncertainties on the extracted value of $\alpha_s(M_Z)$ were considered:

- terms beyond NLO were estimated by varying μ_R between $Q/2$ and $2Q$ and keeping μ_F fixed at Q ; this results in a variation of $\Delta\alpha_s(M_Z) = {}^{+0.0089}_{-0.0070}$;

- the uncertainty on the modelling of the parton shower was estimated by using the MEPS model to calculate the parton-to-hadron correction factors; this results in a variation of $\Delta\alpha_s(M_Z) = 0.0018$;
- the uncertainty in the choice of μ_R was estimated by using $\mu_R = E_T^{\text{jet}}$ instead of Q and μ_F was set to Q ; this results in a variation of $\Delta\alpha_s(M_Z) = 0.0003$;
- the uncertainty in the NLO QCD calculations due to the uncertainties in the proton PDFs was estimated by repeating the calculations using 40 additional sets from CTEQ6 [53]; this results in a variation of $\Delta\alpha_s(M_Z) = 0.0002$;
- the uncertainty of the calculations in the value of μ_F was estimated by repeating the calculations with $\mu_F = Q/2$ and $2Q$; this results in a variation of $\Delta\alpha_s(M_Z) = 0.0001$.

These uncertainties were added in quadrature and give a total theoretical uncertainty of $\Delta\alpha_s(M_Z)/\alpha_s(M_Z) = {}^{+7.7}_{-6.1}\%$. As a cross-check of the extracted value of $\alpha_s(M_Z)$, the fit procedure was repeated by using the five sets of the CTEQ4 “A-series”, resulting in $\alpha_s(M_Z) = 0.1178 \pm 0.0009$, in very good agreement with the central value determined above. As a consistency check, the whole procedure was repeated for $\langle\psi(r = 0.4)\rangle$ and $\langle\psi(r = 0.6)\rangle$, giving values of $\alpha_s(M_Z) = 0.1158 \pm 0.0008$ and $\alpha_s(M_Z) = 0.1193 \pm 0.0010$, respectively, which are compatible with the value determined from $\langle\psi(r = 0.5)\rangle$. The determination of $\alpha_s(M_Z)$ was also repeated using the calculations from the DISASTER++ program; this gave $\alpha_s(M_Z) = 0.1166 \pm 0.0009$, which is compatible with the value quoted above.

The value of $\alpha_s(M_Z)$ as determined from the measured $\langle\psi(r = 0.5)\rangle$ is therefore

$$\alpha_s(M_Z) = 0.1176 \pm 0.0009 \text{ (stat.) } {}^{+0.0009}_{-0.0026} \text{ (exp.) } {}^{+0.0091}_{-0.0072} \text{ (th.)}.$$

This result is in agreement with recent determinations using measurements of jet production in DIS [1, 4, 6, 8, 27] and photoproduction [5] and with the current world average of 0.1183 ± 0.0027 [54]. This determination of α_s has experimental uncertainties as small as those based on previous measurements. However, the theoretical uncertainty is large and dominated by terms beyond NLO. Further theoretical work on higher-order contributions would allow an improved determination of α_s from the integrated jet shape in DIS.

10 Summary and conclusions

Measurements of the mean integrated jet shape and mean subjet multiplicities for inclusive jet photoproduction and DIS at a centre-of-mass energy of 318 GeV using the data collected by ZEUS in 1998 to 2000, which correspond to an integrated luminosity of 82.2 pb^{-1} , have been presented. The measurements refer to jets identified with the k_T

cluster algorithm in the longitudinally invariant inclusive mode in the laboratory frame and selected according to $E_T^{\text{jet}} > 17$ GeV and $-1 < \eta^{\text{jet}} < 2.5$. The measurements are given in the kinematic region defined by $Q^2 < 1$ GeV² and $142 < W_{\gamma p} < 293$ GeV for photoproduction and $Q^2 > 125$ GeV² for DIS. The jet shape broadens (narrows) and the mean subjet multiplicity increases (decreases) as η^{jet} (E_T^{jet}) increases in photoproduction. The observed broadening of the jet shape and the increase of the mean subjet multiplicity as η^{jet} increases are consistent with an increase of the fraction of gluon-initiated jets. In DIS, the data show no significant dependence with η^{jet} and a moderate dependence with E_T^{jet} . Leading-logarithm parton-shower MC models for photoproduction and NLO QCD calculations for DIS give a good description of the data.

Measurements of differential inclusive jet and dijet cross sections in the photoproduction and DIS regimes separated into broad and narrow jets according to their internal structure have been presented. Leading-logarithm parton-shower MC models give a good description of the data. The inclusive jet cross-sections $d\sigma/d\eta^{\text{jet}}$ and $d\sigma/dE_T^{\text{jet}}$ for broad- and narrow-jet samples show the expected behaviour for samples enriched in gluon- and quark-initiated jets, respectively. The dijet cross section as a function of $|\cos\theta^*|$, measured in the range $|\cos\theta^*| < 0.8$ and integrated over $M^{\text{jj}} > 52$ GeV, displays for broad-broad dijets a behaviour consistent with that expected for a sample enriched in processes mediated by gluon exchange. Narrow-narrow dijets, however, show a behaviour consistent with a sample enriched in processes mediated by quark exchange. The dijet cross-section $d\sigma/d\cos\theta_{\text{broad}}^*$, measured in the region $-0.8 < \cos\theta_{\text{broad}}^* < 0.8$ and integrated over $M^{\text{jj}} > 52$ GeV, for a sample of events with broad-narrow dijets, exhibits a large asymmetry consistent with the expected dominance of gluon (quark) exchange as $\cos\theta_{\text{broad}}^* \rightarrow +1$ ($\cos\theta_{\text{broad}}^* \rightarrow -1$). The dijet cross section as a function of M^{jj} and x_{γ}^{obs} for the sample of broad-broad dijets shows a behaviour consistent with the dominance of the resolved $q_{\gamma}g_p \rightarrow qg$ subprocess, whereas the sample with narrow-narrow dijets is consistent with the dominance of the direct subprocess $\gamma g \rightarrow q\bar{q}$.

The measurements of the mean integrated jet shape in DIS have been used to extract a value of $\alpha_s(M_Z)$ by comparing to the predictions of NLO QCD as a function of E_T^{jet} . The calculations reproduce the measured observables well, demonstrating the validity of the description of the internal structure of jets by pQCD. The value of $\alpha_s(M_Z)$ as determined by fitting the NLO QCD calculations to the measured mean integrated jet shape $\langle\psi(r=0.5)\rangle$ for $E_T^{\text{jet}} > 21$ GeV is

$$\alpha_s(M_Z) = 0.1176 \pm 0.0009 \text{ (stat.) } {}^{+0.0009}_{-0.0026} \text{ (exp.) } {}^{+0.0091}_{-0.0072} \text{ (th.)}.$$

This value is in good agreement with the current world average.

Acknowledgements

We thank the DESY Directorate for their strong support and encouragement. The remarkable achievements of the HERA machine group were essential for the successful completion of this work and are greatly appreciated. We would like to thank M. Seymour for useful discussions.

References

- [1] ZEUS Coll., J. Breitweg et al., Phys. Lett. B 507 (2001) 70.
- [2] ZEUS Coll., S. Chekanov et al., Phys. Lett. B 531 (2002) 9.
- [3] ZEUS Coll., S. Chekanov et al., Eur. Phys. J. C 23 (2002) 615.
- [4] ZEUS Coll., S. Chekanov et al., Phys. Lett. B 547 (2002) 164.
- [5] ZEUS Coll., S. Chekanov et al., Phys. Lett. B 560 (2003) 7.
- [6] ZEUS Coll., J. Chekanov et al., Eur. Phys. J. C 31 (2003) 149.
- [7] ZEUS Coll., S. Chekanov et al., Eur. Phys. J. C 23 (2002) 13;
ZEUS Coll., J. Breitweg et al., Phys. Lett. B 443 (1998) 394.
- [8] H1 Coll., C. Adloff et al., Eur. Phys. J. C 19 (2001) 289.
- [9] H1 Coll., C. Adloff et al., Eur. Phys. J. C 25 (2002) 13;
H1 Coll., C. Adloff et al., Phys. Lett. B 542 (2002) 193;
H1 Coll., C. Adloff et al., Eur. Phys. J. C 29 (2003) 497;
H1 Coll., C. Adloff et al., Eur. Phys. J. C 19 (2001) 429;
H1 Coll., C. Adloff et al., Phys. Lett. B 515 (2001) 17.
- [10] ZEUS Coll., S. Chekanov et al., Phys. Lett. B 565 (2003) 87;
ZEUS Coll., S. Chekanov et al., Preprint DESY-03-212 (hep-ex/0312057), DESY, 2003.
- [11] C.H. Llewellyn Smith, Phys. Lett. B 79 (1978) 83;
I. Kang and C.H. Llewellyn Smith, Nucl. Phys. B 166 (1980) 413;
J.F. Owens, Phys. Rev. D 21 (1980) 54;
M. Fontannaz, A. Mantrach and D. Schiff, Z. Phys. C 6 (1980) 241.
- [12] W.J. Stirling and Z. Kunszt, *Proc. HERA Workshop*, R.D. Peccei (ed.), Vol. 2, p. 331. DESY, Hamburg, Germany (1987);
M. Drees and F. Halzen, Phys. Rev. Lett. 61 (1988) 275;
M. Drees and R.M. Godbole, Phys. Rev. Lett. 61 (1988) 682;
M. Drees and R.M. Godbole, Phys. Rev. D 39 (1989) 169;
H. Baer, J. Ohnemus and J.F. Owens, Z. Phys. C 42 (1989) 657;
H. Baer, J. Ohnemus and J.F. Owens, Phys. Rev. D 40 (1989) 2844.
- [13] S.D. Ellis, Z. Kunszt and D.E. Soper, Phys. Rev. Lett. 69 (1992) 3615.
- [14] S. Catani et al., Nucl. Phys. B 383 (1992) 419;
M.H. Seymour, Nucl. Phys. B 421 (1994) 545;
M.H. Seymour, Phys. Lett. B 378 (1996) 279;
J.R. Forshaw and M.H. Seymour, JHEP 9909 (1999) 009.

- [15] ZEUS Coll., M. Derrick et al., *Phys. Lett. B* 384 (1996) 401.
- [16] S. Catani et al., *Nucl. Phys. B* 406 (1993) 187.
- [17] S.D. Ellis and D.E. Soper, *Phys. Rev. D* 48 (1993) 3160.
- [18] ZEUS Coll., M. Derrick et al., *Phys. Lett. B* 293 (1992) 465.
- [19] ZEUS Coll., U. Holm (ed.), *The ZEUS Detector*. Status Report (unpublished), DESY (1993), available on <http://www-zeus.desy.de/bluebook/bluebook.html>.
- [20] N. Harnew et al., *Nucl. Instr. Meth. A* 279 (1989) 290;
B. Foster et al., *Nucl. Phys. Proc. Suppl. B* 32 (1993) 181;
B. Foster et al., *Nucl. Instr. Meth. A* 338 (1994) 254.
- [21] M. Derrick et al., *Nucl. Instr. Meth. A* 309 (1991) 77;
A. Andresen et al., *Nucl. Instr. Meth. A* 309 (1991) 101;
A. Caldwell et al., *Nucl. Instr. Meth. A* 321 (1992) 356;
A. Bernstein et al., *Nucl. Instr. Meth. A* 336 (1993) 23.
- [22] J. Andrusków et al., Preprint DESY-92-066, DESY, 1992;
ZEUS Coll., M. Derrick et al., *Z. Phys. C* 63 (1994) 391;
J. Andrusków et al., *Acta Phys. Pol. B* 32 (2001) 2025.
- [23] W.H. Smith, K. Tokushuku and L.W. Wiggers, *Proc. Computing in High-Energy Physics (CHEP), Annecy, France, Sept. 1992*, C. Verkerk and W. Wojcik (eds.), p. 222. CERN, Geneva, Switzerland (1992). Also in preprint DESY 92-150B.
- [24] H. Abramowicz, A. Caldwell and R. Sinkus, *Nucl. Instr. Meth. A* 365 (1995) 508;
R. Sinkus and T. Voss, *Nucl. Instr. Meth. A* 391 (1997) 360.
- [25] ZEUS Coll., M. Derrick et al., *Phys. Lett. B* 322 (1994) 287.
- [26] F. Jacquet and A. Blondel, *Proc. of the Study for an ep Facility for Europe*, U. Amaldi (ed.), p. 391. Hamburg, Germany (1979). Also in preprint DESY 79/48.
- [27] ZEUS Coll., S. Chekanov et al., *Phys. Lett. B* 558 (2003) 41.
- [28] S. Bentvelsen, J. Engelen and P. Kooijman, *Proc. of the Workshop on Physics at HERA*, W. Buchmüller and G. Ingelman (eds.), Vol. 1, p. 23. Hamburg, Germany, DESY (1992);
K.C. Höger, *ibid.*, p. 43.
- [29] J.E. Huth et al., *Research Directions for the Decade. Proc. of Summer Study on High Energy Physics, 1990*, E.L. Berger (ed.), p. 134. World Scientific (1992). Also in preprint FERMILAB-CONF-90-249-E.
- [30] T. Sjöstrand, *Comput. Phys. Comm.* 82 (1994) 74;
T. Sjöstrand et al., *Comput. Phys. Comm.* 135 (2001) 238.

- [31] G. Marchesini et al., *Comput. Phys. Comm.* 67 (1992) 465;
G. Corcella et al., *JHEP* 0101 (2001) 010.
- [32] M. Glück, E. Reya and A. Vogt, *Phys. Rev. D* 45 (1992) 3986;
M. Glück, E. Reya and A. Vogt, *Phys. Rev. D* 46 (1992) 1973.
- [33] H.L. Lai et al., *Phys. Rev. D* 55 (1997) 1280.
- [34] B. Andersson et al., *Phys. Rep.* 97 (1983) 31.
- [35] T. Sjöstrand, *Comput. Phys. Comm.* 39 (1986) 347;
T. Sjöstrand and M. Bengtsson, *Comput. Phys. Comm.* 43 (1987) 367.
- [36] B.R. Webber, *Nucl. Phys. B* 238 (1984) 492.
- [37] T. Sjöstrand and M. van Zijl, *Phys. Rev. D* 36 (1987) 2019.
- [38] ZEUS Coll., J. Breitweg et al., *Eur. Phys. J. C* 2 (1998) 61.
- [39] A. Kwiatkowski, H. Spiesberger and H.-J. Möhring, *Comput. Phys. Comm.* 69 (1992) 155;
H. Spiesberger, *An Event Generator for ep Interactions at HERA Including Radiative Processes (Version 4.6)*, 1996, available on
<http://www.desy.de/~hspiesb/heracles.html>.
- [40] K. Charuła, G.A. Schuler and H. Spiesberger, *Comput. Phys. Comm.* 81 (1994) 381;
H. Spiesberger, *HERACLES and DJANGO: Event Generation for ep Interactions at HERA Including Radiative Processes*, 1998, available on
<http://www.desy.de/~hspiesb/djangoh.html>.
- [41] Y. Azimov et al., *Phys. Lett. B* 165 (1985) 147;
G. Gustafson, *Phys. Lett. B* 175 (1986) 453;
G. Gustafson and U. Pettersson, *Nucl. Phys. B* 306 (1988) 746;
B. Andersson et al., *Z. Phys. C* 43 (1989) 625.
- [42] L. Lönnblad, *Comput. Phys. Comm.* 71 (1992) 15;
L. Lönnblad, *Z. Phys. C* 65 (1995) 285.
- [43] G. Ingelman, A. Edin and J. Rathsman, *Comput. Phys. Comm.* 101 (1997) 108.
- [44] H.L. Lai et al., *Eur. Phys. J. C* 12 (2000) 375.
- [45] R. Brun et al., *GEANT3*, Technical Report CERN-DD/EE/84-1, CERN, 1987.
- [46] S. Catani and M.H. Seymour, *Nucl. Phys. B* 485 (1997) 291. Erratum in *Nucl. Phys. B* 510 (1998) 503. .
- [47] R.K. Ellis, D.A. Ross and A.E. Terrano, *Nucl. Phys. B* 178 (1981) 421.
- [48] A.D. Martin et al., *Eur. Phys. J. C* 4 (1998) 463;
A.D. Martin et al., *Eur. Phys. J. C* 14 (2000) 133.

- [49] D. Graudenz, *Proc. of the Ringberg Workshop on New Trends in HERA physics*, B.A. Kniehl, G. Krämer and A. Wagner (eds.). World Scientific, Singapore (1998). Also in hep-ph/9708362 (1997);
D. Graudenz, Preprint hep-ph/9710244, 1997.
- [50] M. Wing (on behalf of the ZEUS Coll.), *Proc. of the 10th International Conference on Calorimetry in High Energy Physics*, R. Zhu (ed.), p. 767. Pasadena, USA (2002). Also in preprint hep-ex/0206036.
- [51] ZEUS Coll., J. Breitweg et al., *Eur. Phys. J. C* 11 (1999) 427.
- [52] ZEUS Coll., J. Breitweg et al., *Eur. Phys. J. C* 8 (1999) 367.
- [53] J. Pumplin et al., *JHEP* 0207 (2002) 012;
D. Stump et al., *JHEP* 0310 (2003) 046.
- [54] S. Bethke, *J. Phys. G* 26 (2000) R27. Updated in Preprint hep-ex/0211012, 2002.

r	$\langle\psi(r)\rangle \pm \text{stat.} \pm \text{syst.}$	
	$-1 < \eta^{\text{jet}} < 0$	$0 < \eta^{\text{jet}} < 1$
0.1	$0.3135 \pm 0.0025^{+0.0033}_{-0.0048}$	$0.3040 \pm 0.0012^{+0.0021}_{-0.0032}$
0.2	$0.5870 \pm 0.0025^{+0.0038}_{-0.0138}$	$0.5730 \pm 0.0012^{+0.0025}_{-0.0100}$
0.3	$0.7322 \pm 0.0020^{+0.0029}_{-0.0106}$	$0.7189 \pm 0.0010^{+0.0019}_{-0.0071}$
0.4	$0.8165 \pm 0.0015^{+0.0021}_{-0.0059}$	$0.8075 \pm 0.0007^{+0.0015}_{-0.0047}$
0.5	$0.8720 \pm 0.0011^{+0.0014}_{-0.0041}$	$0.8649 \pm 0.0006^{+0.0010}_{-0.0024}$
0.6	$0.9106 \pm 0.0008^{+0.0010}_{-0.0025}$	$0.9048 \pm 0.0004^{+0.0008}_{-0.0015}$
0.7	$0.9382 \pm 0.0006^{+0.0006}_{-0.0020}$	$0.9335 \pm 0.0003^{+0.0005}_{-0.0007}$
0.8	$0.9577 \pm 0.0004^{+0.0005}_{-0.0009}$	$0.9541 \pm 0.0002^{+0.0003}_{-0.0004}$
0.9	$0.9719 \pm 0.0003^{+0.0003}_{-0.0007}$	$0.9690 \pm 0.0002^{+0.0002}_{-0.0003}$
1.0	$0.9817 \pm 0.0002^{+0.0003}_{-0.0003}$	$0.9797 \pm 0.0001^{+0.0002}_{-0.0002}$

r	$\langle\psi(r)\rangle \pm \text{stat.} \pm \text{syst.}$	
	$1 < \eta^{\text{jet}} < 1.5$	$1.5 < \eta^{\text{jet}} < 2.5$
0.1	$0.2678 \pm 0.0016^{+0.0038}_{-0.0026}$	$0.2236 \pm 0.0012^{+0.0084}_{-0.0019}$
0.2	$0.5238 \pm 0.0018^{+0.0030}_{-0.0038}$	$0.4581 \pm 0.0013^{+0.0039}_{-0.0023}$
0.3	$0.6740 \pm 0.0016^{+0.0025}_{-0.0025}$	$0.6121 \pm 0.0012^{+0.0041}_{-0.0022}$
0.4	$0.7721 \pm 0.0012^{+0.0019}_{-0.0020}$	$0.7180 \pm 0.0010^{+0.0044}_{-0.0020}$
0.5	$0.8378 \pm 0.0009^{+0.0017}_{-0.0015}$	$0.7936 \pm 0.0008^{+0.0033}_{-0.0017}$
0.6	$0.8848 \pm 0.0007^{+0.0013}_{-0.0011}$	$0.8488 \pm 0.0006^{+0.0030}_{-0.0013}$
0.7	$0.9191 \pm 0.0005^{+0.0010}_{-0.0008}$	$0.8903 \pm 0.0005^{+0.0026}_{-0.0010}$
0.8	$0.9436 \pm 0.0004^{+0.0009}_{-0.0006}$	$0.9215 \pm 0.0004^{+0.0023}_{-0.0007}$
0.9	$0.9619 \pm 0.0003^{+0.0007}_{-0.0004}$	$0.9457 \pm 0.0003^{+0.0015}_{-0.0005}$
1.0	$0.9749 \pm 0.0002^{+0.0005}_{-0.0003}$	$0.9637 \pm 0.0002^{+0.0009}_{-0.0003}$

Table 1: Measured mean integrated jet shape corrected to the hadron level for jets in photoproduction with $E_T^{\text{jet}} > 17$ GeV in different η^{jet} regions. The statistical and systematic uncertainties are also indicated.

r	$\langle\psi(r)\rangle \pm \text{stat.} \pm \text{syst.}$	
	$17 < E_T^{\text{jet}} < 21 \text{ GeV}$	$21 < E_T^{\text{jet}} < 25 \text{ GeV}$
0.1	$0.2406 \pm 0.0009^{+0.0054}_{-0.0019}$	$0.2915 \pm 0.0016^{+0.0033}_{-0.0027}$
0.2	$0.4934 \pm 0.0010^{+0.0021}_{-0.0025}$	$0.5470 \pm 0.0017^{+0.0030}_{-0.0037}$
0.3	$0.6477 \pm 0.0009^{+0.0019}_{-0.0020}$	$0.6938 \pm 0.0014^{+0.0026}_{-0.0026}$
0.4	$0.7489 \pm 0.0007^{+0.0023}_{-0.0017}$	$0.7857 \pm 0.0011^{+0.0019}_{-0.0018}$
0.5	$0.8188 \pm 0.0006^{+0.0025}_{-0.0013}$	$0.8469 \pm 0.0009^{+0.0014}_{-0.0013}$
0.6	$0.8691 \pm 0.0004^{+0.0024}_{-0.0010}$	$0.8901 \pm 0.0007^{+0.0012}_{-0.0010}$
0.7	$0.9064 \pm 0.0003^{+0.0022}_{-0.0007}$	$0.9217 \pm 0.0005^{+0.0009}_{-0.0007}$
0.8	$0.9338 \pm 0.0003^{+0.0018}_{-0.0005}$	$0.9447 \pm 0.0004^{+0.0011}_{-0.0006}$
0.9	$0.9547 \pm 0.0002^{+0.0013}_{-0.0003}$	$0.9621 \pm 0.0003^{+0.0009}_{-0.0004}$
1.0	$0.9698 \pm 0.0001^{+0.0009}_{-0.0002}$	$0.9746 \pm 0.0002^{+0.0006}_{-0.0003}$

r	$\langle\psi(r)\rangle \pm \text{stat.} \pm \text{syst.}$	
	$25 < E_T^{\text{jet}} < 29 \text{ GeV}$	$29 < E_T^{\text{jet}} < 35 \text{ GeV}$
0.1	$0.3308 \pm 0.0028^{+0.0053}_{-0.0033}$	$0.3616 \pm 0.0039^{+0.0047}_{-0.0050}$
0.2	$0.5897 \pm 0.0027^{+0.0037}_{-0.0037}$	$0.6148 \pm 0.0037^{+0.0043}_{-0.0062}$
0.3	$0.7243 \pm 0.0022^{+0.0038}_{-0.0028}$	$0.7468 \pm 0.0029^{+0.0033}_{-0.0047}$
0.4	$0.8094 \pm 0.0017^{+0.0028}_{-0.0022}$	$0.8279 \pm 0.0022^{+0.0026}_{-0.0037}$
0.5	$0.8653 \pm 0.0013^{+0.0029}_{-0.0017}$	$0.8792 \pm 0.0016^{+0.0019}_{-0.0023}$
0.6	$0.9041 \pm 0.0010^{+0.0020}_{-0.0013}$	$0.9146 \pm 0.0012^{+0.0015}_{-0.0016}$
0.7	$0.9322 \pm 0.0008^{+0.0021}_{-0.0009}$	$0.9402 \pm 0.0010^{+0.0012}_{-0.0012}$
0.8	$0.9528 \pm 0.0006^{+0.0018}_{-0.0006}$	$0.9578 \pm 0.0007^{+0.0008}_{-0.0008}$
0.9	$0.9675 \pm 0.0004^{+0.0018}_{-0.0005}$	$0.9713 \pm 0.0006^{+0.0006}_{-0.0007}$
1.0	$0.9783 \pm 0.0003^{+0.0012}_{-0.0004}$	$0.9807 \pm 0.0004^{+0.0005}_{-0.0005}$

Table 2: Measured mean integrated jet shape corrected to the hadron level for jets in photoproduction with $-1 < \eta^{\text{jet}} < 2.5$ in different E_T^{jet} regions. The statistical and systematic uncertainties are also indicated.

r	$\langle\psi(r)\rangle \pm \text{stat.} \pm \text{syst.}$	
	$35 < E_T^{\text{jet}} < 41 \text{ GeV}$	$41 < E_T^{\text{jet}} < 47 \text{ GeV}$
0.1	$0.4045 \pm 0.0068^{+0.0069}_{-0.0068}$	$0.431 \pm 0.012^{+0.013}_{-0.014}$
0.2	$0.6538 \pm 0.0061^{+0.0063}_{-0.0067}$	$0.681 \pm 0.010^{+0.012}_{-0.010}$
0.3	$0.7792 \pm 0.0047^{+0.0049}_{-0.0060}$	$0.7960 \pm 0.0078^{+0.0091}_{-0.0080}$
0.4	$0.8491 \pm 0.0035^{+0.0037}_{-0.0041}$	$0.8607 \pm 0.0058^{+0.0080}_{-0.0059}$
0.5	$0.8959 \pm 0.0026^{+0.0029}_{-0.0026}$	$0.9019 \pm 0.0042^{+0.0052}_{-0.0043}$
0.6	$0.9279 \pm 0.0019^{+0.0021}_{-0.0020}$	$0.9326 \pm 0.0030^{+0.0050}_{-0.0030}$
0.7	$0.9494 \pm 0.0015^{+0.0016}_{-0.0016}$	$0.9539 \pm 0.0022^{+0.0024}_{-0.0023}$
0.8	$0.9644 \pm 0.0011^{+0.0012}_{-0.0012}$	$0.9677 \pm 0.0017^{+0.0023}_{-0.0017}$
0.9	$0.9758 \pm 0.0009^{+0.0010}_{-0.0009}$	$0.9778 \pm 0.0013^{+0.0014}_{-0.0013}$
1.0	$0.9835 \pm 0.0007^{+0.0008}_{-0.0007}$	$0.9850 \pm 0.0010^{+0.0010}_{-0.0011}$
r	$\langle\psi(r)\rangle \pm \text{stat.} \pm \text{syst.}$	
	$47 < E_T^{\text{jet}} < 55 \text{ GeV}$	$55 < E_T^{\text{jet}} < 71 \text{ GeV}$
0.1	$0.484 \pm 0.019^{+0.020}_{-0.031}$	$0.449 \pm 0.027^{+0.071}_{-0.028}$
0.2	$0.716 \pm 0.015^{+0.016}_{-0.015}$	$0.687 \pm 0.025^{+0.036}_{-0.025}$
0.3	$0.829 \pm 0.011^{+0.012}_{-0.016}$	$0.787 \pm 0.019^{+0.037}_{-0.019}$
0.4	$0.8892 \pm 0.0082^{+0.0083}_{-0.0199}$	$0.858 \pm 0.014^{+0.020}_{-0.014}$
0.5	$0.9221 \pm 0.0060^{+0.0061}_{-0.0140}$	$0.900 \pm 0.010^{+0.013}_{-0.010}$
0.6	$0.9441 \pm 0.0043^{+0.0045}_{-0.0077}$	$0.9328 \pm 0.0074^{+0.0080}_{-0.0075}$
0.7	$0.9607 \pm 0.0033^{+0.0035}_{-0.0055}$	$0.9513 \pm 0.0053^{+0.0056}_{-0.0053}$
0.8	$0.9730 \pm 0.0025^{+0.0026}_{-0.0046}$	$0.9700 \pm 0.0038^{+0.0040}_{-0.0045}$
0.9	$0.9805 \pm 0.0019^{+0.0020}_{-0.0036}$	$0.9795 \pm 0.0028^{+0.0030}_{-0.0046}$
1.0	$0.9867 \pm 0.0015^{+0.0016}_{-0.0023}$	$0.9863 \pm 0.0022^{+0.0023}_{-0.0056}$

Table 3: Measured mean integrated jet shape corrected to the hadron level for jets in photoproduction with $-1 < \eta^{\text{jet}} < 2.5$ in different E_T^{jet} regions. The statistical and systematic uncertainties are also indicated.

r	$\langle\psi(r)\rangle \pm \text{stat.} \pm \text{syst.}$	
	$-1 < \eta^{\text{jet}} < 0$	$0 < \eta^{\text{jet}} < 1$
0.1	$0.3434 \pm 0.0034^{+0.0199}_{-0.0037}$	$0.3759 \pm 0.0019^{+0.0028}_{-0.0070}$
0.2	$0.6332 \pm 0.0030^{+0.0128}_{-0.0033}$	$0.6487 \pm 0.0016^{+0.0027}_{-0.0073}$
0.3	$0.7720 \pm 0.0022^{+0.0075}_{-0.0024}$	$0.7811 \pm 0.0012^{+0.0019}_{-0.0071}$
0.4	$0.8474 \pm 0.0016^{+0.0041}_{-0.0017}$	$0.8542 \pm 0.0009^{+0.0013}_{-0.0048}$
0.5	$0.8950 \pm 0.0011^{+0.0031}_{-0.0012}$	$0.8999 \pm 0.0006^{+0.0009}_{-0.0031}$
0.6	$0.9271 \pm 0.0008^{+0.0023}_{-0.0008}$	$0.9309 \pm 0.0005^{+0.0006}_{-0.0029}$
0.7	$0.9496 \pm 0.0006^{+0.0018}_{-0.0006}$	$0.9528 \pm 0.0003^{+0.0004}_{-0.0023}$
0.8	$0.9659 \pm 0.0005^{+0.0009}_{-0.0005}$	$0.9683 \pm 0.0002^{+0.0003}_{-0.0016}$
0.9	$0.9780 \pm 0.0003^{+0.0007}_{-0.0003}$	$0.9793 \pm 0.0002^{+0.0002}_{-0.0014}$
1.0	$0.9863 \pm 0.0002^{+0.0003}_{-0.0004}$	$0.9868 \pm 0.0001^{+0.0001}_{-0.0009}$

r	$\langle\psi(r)\rangle \pm \text{stat.} \pm \text{syst.}$	
	$1 < \eta^{\text{jet}} < 1.5$	$1.5 < \eta^{\text{jet}} < 2.5$
0.1	$0.3880 \pm 0.0026^{+0.0042}_{-0.0052}$	$0.3964 \pm 0.0023^{+0.0032}_{-0.0055}$
0.2	$0.6585 \pm 0.0023^{+0.0037}_{-0.0034}$	$0.6660 \pm 0.0018^{+0.0030}_{-0.0039}$
0.3	$0.7879 \pm 0.0018^{+0.0032}_{-0.0026}$	$0.7922 \pm 0.0013^{+0.0029}_{-0.0037}$
0.4	$0.8589 \pm 0.0013^{+0.0025}_{-0.0018}$	$0.8612 \pm 0.0010^{+0.0029}_{-0.0028}$
0.5	$0.9039 \pm 0.0009^{+0.0020}_{-0.0019}$	$0.9048 \pm 0.0007^{+0.0025}_{-0.0018}$
0.6	$0.9343 \pm 0.0007^{+0.0015}_{-0.0017}$	$0.9345 \pm 0.0006^{+0.0021}_{-0.0018}$
0.7	$0.9556 \pm 0.0005^{+0.0011}_{-0.0016}$	$0.9553 \pm 0.0004^{+0.0018}_{-0.0012}$
0.8	$0.9700 \pm 0.0004^{+0.0007}_{-0.0012}$	$0.9700 \pm 0.0003^{+0.0015}_{-0.0012}$
0.9	$0.9804 \pm 0.0003^{+0.0006}_{-0.0009}$	$0.9803 \pm 0.0003^{+0.0012}_{-0.0009}$
1.0	$0.9876 \pm 0.0002^{+0.0004}_{-0.0007}$	$0.9874 \pm 0.0002^{+0.0009}_{-0.0005}$

Table 4: Measured mean integrated jet shape corrected to the hadron level and for electroweak radiative effects for jets in DIS with $E_T^{\text{jet}} > 17$ GeV in different η^{jet} regions. The statistical and systematic uncertainties are also indicated.

r	$\langle\psi(r)\rangle \pm \text{stat.} \pm \text{syst.}$	
	$17 < E_T^{\text{jet}} < 21 \text{ GeV}$	$21 < E_T^{\text{jet}} < 25 \text{ GeV}$
0.1	$0.3211 \pm 0.0016^{+0.0034}_{-0.0067}$	$0.3817 \pm 0.0025^{+0.0054}_{-0.0070}$
0.2	$0.6093 \pm 0.0015^{+0.0031}_{-0.0044}$	$0.6588 \pm 0.0022^{+0.0047}_{-0.0028}$
0.3	$0.7547 \pm 0.0012^{+0.0024}_{-0.0031}$	$0.7881 \pm 0.0016^{+0.0028}_{-0.0018}$
0.4	$0.8351 \pm 0.0009^{+0.0017}_{-0.0022}$	$0.8587 \pm 0.0012^{+0.0028}_{-0.0013}$
0.5	$0.8866 \pm 0.0007^{+0.0013}_{-0.0012}$	$0.9030 \pm 0.0009^{+0.0020}_{-0.0009}$
0.6	$0.9216 \pm 0.0005^{+0.0011}_{-0.0014}$	$0.9330 \pm 0.0007^{+0.0014}_{-0.0008}$
0.7	$0.9465 \pm 0.0004^{+0.0009}_{-0.0012}$	$0.9541 \pm 0.0005^{+0.0011}_{-0.0005}$
0.8	$0.9640 \pm 0.0003^{+0.0008}_{-0.0010}$	$0.9691 \pm 0.0004^{+0.0007}_{-0.0004}$
0.9	$0.9766 \pm 0.0002^{+0.0006}_{-0.0009}$	$0.9796 \pm 0.0003^{+0.0006}_{-0.0003}$
1.0	$0.9852 \pm 0.0002^{+0.0005}_{-0.0006}$	$0.9870 \pm 0.0002^{+0.0004}_{-0.0002}$
r	$\langle\psi(r)\rangle \pm \text{stat.} \pm \text{syst.}$	
	$25 < E_T^{\text{jet}} < 29 \text{ GeV}$	$29 < E_T^{\text{jet}} < 35 \text{ GeV}$
0.1	$0.4312 \pm 0.0036^{+0.0095}_{-0.0065}$	$0.4797 \pm 0.0044^{+0.0055}_{-0.0089}$
0.2	$0.6949 \pm 0.0030^{+0.0047}_{-0.0044}$	$0.7239 \pm 0.0034^{+0.0036}_{-0.0043}$
0.3	$0.8107 \pm 0.0022^{+0.0040}_{-0.0032}$	$0.8281 \pm 0.0025^{+0.0028}_{-0.0032}$
0.4	$0.8733 \pm 0.0016^{+0.0038}_{-0.0024}$	$0.8863 \pm 0.0018^{+0.0020}_{-0.0025}$
0.5	$0.9131 \pm 0.0011^{+0.0026}_{-0.0016}$	$0.9225 \pm 0.0013^{+0.0015}_{-0.0018}$
0.6	$0.9399 \pm 0.0008^{+0.0021}_{-0.0011}$	$0.9471 \pm 0.0009^{+0.0011}_{-0.0015}$
0.7	$0.9590 \pm 0.0006^{+0.0016}_{-0.0008}$	$0.9639 \pm 0.0007^{+0.0010}_{-0.0015}$
0.8	$0.9725 \pm 0.0005^{+0.0013}_{-0.0007}$	$0.9754 \pm 0.0005^{+0.0007}_{-0.0013}$
0.9	$0.9818 \pm 0.0004^{+0.0010}_{-0.0005}$	$0.9839 \pm 0.0004^{+0.0005}_{-0.0009}$
1.0	$0.9885 \pm 0.0003^{+0.0007}_{-0.0003}$	$0.9895 \pm 0.0003^{+0.0004}_{-0.0008}$

Table 5: Measured mean integrated jet shape corrected to the hadron level and for electroweak radiative effects for jets in DIS with $-1 < \eta^{\text{jet}} < 2.5$ in different E_T^{jet} regions. The statistical and systematic uncertainties are also indicated.

r	$\langle\psi(r)\rangle \pm \text{stat.} \pm \text{syst.}$	
	$35 < E_T^{\text{jet}} < 41 \text{ GeV}$	$41 < E_T^{\text{jet}} < 47 \text{ GeV}$
0.1	$0.5194 \pm 0.0067^{+0.0128}_{-0.0075}$	$0.5630 \pm 0.0095^{+0.0144}_{-0.0100}$
0.2	$0.7503 \pm 0.0049^{+0.0095}_{-0.0058}$	$0.7755 \pm 0.0066^{+0.0087}_{-0.0071}$
0.3	$0.8464 \pm 0.0035^{+0.0068}_{-0.0038}$	$0.8629 \pm 0.0047^{+0.0058}_{-0.0049}$
0.4	$0.8990 \pm 0.0025^{+0.0038}_{-0.0027}$	$0.9110 \pm 0.0033^{+0.0046}_{-0.0048}$
0.5	$0.9305 \pm 0.0018^{+0.0030}_{-0.0019}$	$0.9395 \pm 0.0023^{+0.0033}_{-0.0042}$
0.6	$0.9530 \pm 0.0013^{+0.0019}_{-0.0013}$	$0.9584 \pm 0.0017^{+0.0023}_{-0.0018}$
0.7	$0.9684 \pm 0.0009^{+0.0016}_{-0.0012}$	$0.9718 \pm 0.0012^{+0.0018}_{-0.0012}$
0.8	$0.9789 \pm 0.0007^{+0.0012}_{-0.0009}$	$0.9806 \pm 0.0009^{+0.0018}_{-0.0009}$
0.9	$0.9861 \pm 0.0005^{+0.0009}_{-0.0006}$	$0.9874 \pm 0.0007^{+0.0011}_{-0.0007}$
1.0	$0.9911 \pm 0.0004^{+0.0007}_{-0.0004}$	$0.9920 \pm 0.0005^{+0.0008}_{-0.0006}$
r	$\langle\psi(r)\rangle \pm \text{stat.} \pm \text{syst.}$	
	$47 < E_T^{\text{jet}} < 55 \text{ GeV}$	$55 < E_T^{\text{jet}} < 71 \text{ GeV}$
0.1	$0.598 \pm 0.012^{+0.016}_{-0.014}$	$0.622 \pm 0.014^{+0.015}_{-0.020}$
0.2	$0.7893 \pm 0.0082^{+0.0166}_{-0.0082}$	$0.8096 \pm 0.0089^{+0.0103}_{-0.0224}$
0.3	$0.8738 \pm 0.0056^{+0.0112}_{-0.0057}$	$0.8885 \pm 0.0060^{+0.0069}_{-0.0155}$
0.4	$0.9188 \pm 0.0038^{+0.0059}_{-0.0038}$	$0.9288 \pm 0.0041^{+0.0050}_{-0.0096}$
0.5	$0.9445 \pm 0.0027^{+0.0039}_{-0.0027}$	$0.9525 \pm 0.0028^{+0.0036}_{-0.0074}$
0.6	$0.9625 \pm 0.0020^{+0.0039}_{-0.0020}$	$0.9687 \pm 0.0020^{+0.0024}_{-0.0049}$
0.7	$0.9739 \pm 0.0014^{+0.0030}_{-0.0014}$	$0.9782 \pm 0.0015^{+0.0019}_{-0.0030}$
0.8	$0.9824 \pm 0.0010^{+0.0021}_{-0.0010}$	$0.9858 \pm 0.0011^{+0.0017}_{-0.0022}$
0.9	$0.9886 \pm 0.0008^{+0.0015}_{-0.0008}$	$0.9904 \pm 0.0009^{+0.0012}_{-0.0011}$
1.0	$0.9929 \pm 0.0006^{+0.0011}_{-0.0006}$	$0.9944 \pm 0.0006^{+0.0009}_{-0.0012}$

Table 6: Measured mean integrated jet shape corrected to the hadron level and for electroweak radiative effects for jets in DIS with $-1 < \eta^{\text{jet}} < 2.5$ in different E_T^{jet} regions. The statistical and systematic uncertainties are also indicated.

y_{cut}	$\langle n_{\text{subject}}(y_{\text{cut}}) \rangle \pm \text{stat.} \pm \text{syst.}$	
	$-1 < \eta^{\text{jet}} < 0$	$0 < \eta^{\text{jet}} < 1$
0.0005	$4.627 \pm 0.011^{+0.013}_{-0.070}$	$4.723 \pm 0.006^{+0.008}_{-0.088}$
0.001	$3.760 \pm 0.009^{+0.013}_{-0.028}$	$3.836 \pm 0.005^{+0.008}_{-0.055}$
0.003	$2.638 \pm 0.007^{+0.009}_{-0.010}$	$2.687 \pm 0.004^{+0.007}_{-0.016}$
0.005	$2.218 \pm 0.006^{+0.010}_{-0.009}$	$2.265 \pm 0.003^{+0.006}_{-0.007}$
0.01	$1.754 \pm 0.005^{+0.016}_{-0.007}$	$1.797 \pm 0.003^{+0.012}_{-0.005}$
0.03	$1.271 \pm 0.004^{+0.029}_{-0.005}$	$1.301 \pm 0.002^{+0.017}_{-0.003}$
0.05	$1.162 \pm 0.003^{+0.014}_{-0.004}$	$1.175 \pm 0.002^{+0.011}_{-0.002}$
0.1	$1.060 \pm 0.002^{+0.003}_{-0.002}$	$1.064 \pm 0.001^{+0.004}_{-0.001}$
y_{cut}	$\langle n_{\text{subject}}(y_{\text{cut}}) \rangle \pm \text{stat.} \pm \text{syst.}$	
	$1 < \eta^{\text{jet}} < 1.5$	$1.5 < \eta^{\text{jet}} < 2.5$
0.0005	$5.022 \pm 0.008^{+0.012}_{-0.147}$	$5.507 \pm 0.006^{+0.009}_{-0.194}$
0.001	$4.085 \pm 0.007^{+0.010}_{-0.110}$	$4.472 \pm 0.005^{+0.009}_{-0.149}$
0.003	$2.860 \pm 0.005^{+0.008}_{-0.059}$	$3.138 \pm 0.004^{+0.009}_{-0.091}$
0.005	$2.399 \pm 0.005^{+0.007}_{-0.031}$	$2.639 \pm 0.003^{+0.007}_{-0.071}$
0.01	$1.912 \pm 0.004^{+0.006}_{-0.012}$	$2.091 \pm 0.003^{+0.005}_{-0.035}$
0.03	$1.383 \pm 0.003^{+0.006}_{-0.005}$	$1.487 \pm 0.002^{+0.005}_{-0.005}$
0.05	$1.231 \pm 0.003^{+0.004}_{-0.004}$	$1.309 \pm 0.002^{+0.004}_{-0.005}$
0.1	$1.092 \pm 0.002^{+0.002}_{-0.002}$	$1.131 \pm 0.002^{+0.002}_{-0.004}$

Table 7: Measured mean subjet multiplicity corrected to the hadron level for jets in photoproduction with $E_T^{\text{jet}} > 17 \text{ GeV}$ in different η^{jet} regions. The statistical and systematic uncertainties are also indicated.

y_{cut}	$\langle n_{\text{subjet}}(y_{\text{cut}}) \rangle \pm \text{stat.} \pm \text{syst.}$	
	$17 < E_T^{\text{jet}} < 21 \text{ GeV}$	$21 < E_T^{\text{jet}} < 25 \text{ GeV}$
0.0005	$5.273 \pm 0.005^{+0.008}_{-0.161}$	$4.966 \pm 0.008^{+0.011}_{-0.129}$
0.001	$4.304 \pm 0.004^{+0.008}_{-0.114}$	$4.011 \pm 0.007^{+0.010}_{-0.099}$
0.003	$3.027 \pm 0.003^{+0.008}_{-0.060}$	$2.799 \pm 0.005^{+0.007}_{-0.051}$
0.005	$2.549 \pm 0.003^{+0.007}_{-0.044}$	$2.344 \pm 0.004^{+0.007}_{-0.029}$
0.01	$2.020 \pm 0.002^{+0.005}_{-0.023}$	$1.856 \pm 0.004^{+0.006}_{-0.008}$
0.03	$1.429 \pm 0.002^{+0.006}_{-0.003}$	$1.348 \pm 0.003^{+0.008}_{-0.005}$
0.05	$1.262 \pm 0.002^{+0.004}_{-0.002}$	$1.211 \pm 0.002^{+0.004}_{-0.004}$
0.1	$1.104 \pm 0.001^{+0.001}_{-0.001}$	$1.088 \pm 0.002^{+0.002}_{-0.002}$

y_{cut}	$\langle n_{\text{subjet}}(y_{\text{cut}}) \rangle \pm \text{stat.} \pm \text{syst.}$	
	$25 < E_T^{\text{jet}} < 29 \text{ GeV}$	$29 < E_T^{\text{jet}} < 35 \text{ GeV}$
0.0005	$4.723 \pm 0.013^{+0.016}_{-0.161}$	$4.442 \pm 0.017^{+0.018}_{-0.088}$
0.001	$3.777 \pm 0.011^{+0.014}_{-0.118}$	$3.545 \pm 0.014^{+0.017}_{-0.063}$
0.003	$2.590 \pm 0.008^{+0.011}_{-0.053}$	$2.454 \pm 0.010^{+0.013}_{-0.045}$
0.005	$2.181 \pm 0.007^{+0.009}_{-0.031}$	$2.049 \pm 0.009^{+0.011}_{-0.015}$
0.01	$1.725 \pm 0.006^{+0.007}_{-0.008}$	$1.642 \pm 0.008^{+0.013}_{-0.010}$
0.03	$1.292 \pm 0.004^{+0.005}_{-0.006}$	$1.256 \pm 0.006^{+0.014}_{-0.006}$
0.05	$1.181 \pm 0.004^{+0.004}_{-0.009}$	$1.161 \pm 0.005^{+0.008}_{-0.005}$
0.1	$1.066 \pm 0.002^{+0.002}_{-0.002}$	$1.062 \pm 0.003^{+0.004}_{-0.003}$

Table 8: Measured mean subjet multiplicity corrected to the hadron level for jets in photoproduction with $-1 < \eta^{\text{jet}} < 2.5$ in different E_T^{jet} regions. The statistical and systematic uncertainties are also indicated.

y_{cut}	$\langle n_{\text{subject}}(y_{\text{cut}}) \rangle \pm \text{stat.} \pm \text{syst.}$	
	$35 < E_T^{\text{jet}} < 41 \text{ GeV}$	$41 < E_T^{\text{jet}} < 47 \text{ GeV}$
0.0005	$4.152 \pm 0.027^{+0.030}_{-0.090}$	$4.000 \pm 0.043^{+0.044}_{-0.235}$
0.001	$3.264 \pm 0.022^{+0.022}_{-0.076}$	$3.128 \pm 0.035^{+0.037}_{-0.123}$
0.003	$2.272 \pm 0.016^{+0.017}_{-0.063}$	$2.148 \pm 0.026^{+0.027}_{-0.062}$
0.005	$1.885 \pm 0.014^{+0.015}_{-0.025}$	$1.805 \pm 0.022^{+0.023}_{-0.036}$
0.01	$1.514 \pm 0.012^{+0.028}_{-0.012}$	$1.484 \pm 0.020^{+0.026}_{-0.022}$
0.03	$1.226 \pm 0.009^{+0.014}_{-0.011}$	$1.202 \pm 0.015^{+0.022}_{-0.015}$
0.05	$1.143 \pm 0.007^{+0.007}_{-0.015}$	$1.113 \pm 0.011^{+0.012}_{-0.012}$
0.1	$1.052 \pm 0.005^{+0.005}_{-0.005}$	$1.045 \pm 0.007^{+0.008}_{-0.013}$

y_{cut}	$\langle n_{\text{subject}}(y_{\text{cut}}) \rangle \pm \text{stat.} \pm \text{syst.}$	
	$47 < E_T^{\text{jet}} < 55 \text{ GeV}$	$55 < E_T^{\text{jet}} < 71 \text{ GeV}$
0.0005	$3.702 \pm 0.063^{+0.063}_{-0.088}$	$3.621 \pm 0.094^{+0.095}_{-0.302}$
0.001	$2.872 \pm 0.051^{+0.051}_{-0.052}$	$2.726 \pm 0.071^{+0.073}_{-0.074}$
0.003	$2.006 \pm 0.037^{+0.037}_{-0.038}$	$1.971 \pm 0.055^{+0.055}_{-0.082}$
0.005	$1.725 \pm 0.033^{+0.035}_{-0.034}$	$1.722 \pm 0.053^{+0.054}_{-0.079}$
0.01	$1.411 \pm 0.029^{+0.030}_{-0.030}$	$1.459 \pm 0.046^{+0.046}_{-0.068}$
0.03	$1.186 \pm 0.023^{+0.023}_{-0.033}$	$1.268 \pm 0.038^{+0.038}_{-0.060}$
0.05	$1.134 \pm 0.018^{+0.018}_{-0.025}$	$1.172 \pm 0.031^{+0.031}_{-0.072}$
0.1	$1.028 \pm 0.009^{+0.012}_{-0.009}$	$1.081 \pm 0.019^{+0.020}_{-0.061}$

Table 9: Measured mean subjet multiplicity corrected to the hadron level for jets in photoproduction with $-1 < \eta^{\text{jet}} < 2.5$ in different E_T^{jet} regions. The statistical and systematic uncertainties are also indicated.

	PYTHIA	HERWIG	CDM	MEPS
jet shape (%)				
gluons	57/48	50/43	43/47	33/65
quarks	84/51	85/55	93/65	97/57
subjet multiplicity (%)				
gluons	56/63	53/56		
quarks	90/23	92/32		
combination (%)				
gluons	61/43	55/37		
quarks	90/22	93/30		

Table 10: *Purity/efficiency of gluon-initiated jets in the broad-jet sample and of quark-initiated jets in the narrow-jet sample from the PYTHIA and HERWIG photoproduction Monte Carlo generated samples and from the CDM and MEPS NC DIS Monte Carlo generated samples.*

jet shape		
	photoproduction	NC DIS
broad	50737	12032
narrow	65038	47549
broad-broad	5744	
narrow-narrow	11826	
broad-narrow	13813	
subjet multiplicity		
	photoproduction	
broad	55750	
narrow	54654	
combination		
	photoproduction	
broad	37213	
narrow	43928	

Table 11: *Number of jets (events) in the inclusive-jet (dijet) photoproduction and NC DIS samples selected according to various methods.*

η^{jet}	$d\sigma/d\eta^{\text{jet}} \pm \text{stat.} \pm \text{syst.} \pm E_T^{\text{jet}} - \text{scale (pb)}$	
	broad jets	narrow jets
-1.0 - -0.5	$7.1 \pm 0.3^{+2.6+0.8}_{-2.6-0.9}$	$20.9 \pm 0.7^{+1.9+1.9}_{-1.9-1.9}$
-0.5 - 0.0	$60.3 \pm 1.1^{+17.6+4.1}_{-17.6-5.0}$	$137.8 \pm 1.7^{+22.2+6.7}_{-22.2-8.5}$
0.0 - 0.5	$130.0 \pm 1.6^{+27.6+7.6}_{-27.6-8.0}$	$274.3 \pm 2.5^{+26.5+10.8}_{-26.4-11.1}$
0.5 - 1.0	$190.8 \pm 2.1^{+20.3+9.5}_{-20.3-10.5}$	$349.0 \pm 2.8^{+32.4+11.9}_{-32.4-11.7}$
1.0 - 1.5	$240.1 \pm 2.5^{+4.6+11.7}_{-4.6-11.6}$	$299.3 \pm 2.7^{+7.0+8.7}_{-7.0-8.5}$
1.5 - 2.0	$259.1 \pm 2.5^{+11.7+12.8}_{-11.7-12.2}$	$227.9 \pm 2.2^{+3.4+6.6}_{-3.4-6.7}$
2.0 - 2.5	$270.8 \pm 2.5^{+17.2+12.7}_{-17.1-14.4}$	$151.7 \pm 1.8^{+4.1+4.9}_{-4.1-5.4}$

Table 12: Measured differential ep cross-section $d\sigma/d\eta^{\text{jet}}$ for inclusive jet photo-production with $E_T^{\text{jet}} > 17$ GeV. The jets have been selected according to their shape into broad and narrow jets. The statistical and systematic uncertainties –not associated with the absolute energy scale of the jets– are also indicated. The systematic uncertainties associated to the absolute energy scale of the jets are quoted separately.

η^{jet}	$d\sigma/d\eta^{\text{jet}} \pm \text{stat.} \pm \text{syst.} \pm E_T^{\text{jet}} - \text{scale (pb)}$	
	broad jets	narrow jets
-1.0 - -0.5	$8.1 \pm 0.3^{+2.0+0.9}_{-2.0-0.9}$	$8.9 \pm 0.3^{+3.6+0.8}_{-3.6-0.8}$
-0.5 - 0.0	$72.1 \pm 1.1^{+14.8+4.4}_{-14.8-5.3}$	$63.8 \pm 0.9^{+26.5+3.1}_{-26.5-4.2}$
0.0 - 0.5	$153.1 \pm 1.6^{+23.6+7.6}_{-23.6-7.9}$	$132.8 \pm 1.4^{+36.1+5.4}_{-36.1-5.7}$
0.5 - 1.0	$218.7 \pm 2.3^{+13.0+9.6}_{-13.0-10.8}$	$171.9 \pm 1.6^{+43.7+6.0}_{-43.7-6.3}$
1.0 - 1.5	$261.4 \pm 2.8^{+8.1+12.0}_{-8.1-11.8}$	$137.4 \pm 1.2^{+33.1+4.6}_{-33.1-4.3}$
1.5 - 2.0	$300.7 \pm 2.9^{+22.3+12.7}_{-22.3-12.6}$	$103.1 \pm 1.1^{+18.8+3.3}_{-18.8-3.6}$
2.0 - 2.5	$315.5 \pm 2.6^{+25.1+13.5}_{-25.1-15.7}$	$62.4 \pm 0.8^{+17.5+2.2}_{-17.5-2.4}$

Table 13: Measured differential ep cross-section $d\sigma/d\eta^{\text{jet}}$ for inclusive jet photo-production with $E_T^{\text{jet}} > 17$ GeV. The jets have been selected according to their subjet multiplicity into broad and narrow jets. The statistical and systematic uncertainties –not associated with the absolute energy scale of the jets– are also indicated. The systematic uncertainties associated to the absolute energy scale of the jets are quoted separately.

η^{jet}	$d\sigma/d\eta^{\text{jet}} \pm \text{stat.} \pm \text{syst.} \pm E_T^{\text{jet}} - \text{scale (pb)}$	
	broad jets	narrow jets
-1.0 – -0.5	$4.7 \pm 0.3^{+1.7+0.5}_{-1.7-0.6}$	$8.5 \pm 0.3^{+2.7+0.7}_{-2.7-0.7}$
-0.5 – 0.0	$44.0 \pm 0.9^{+10.1+3.0}_{-10.1-3.7}$	$58.8 \pm 0.9^{+22.1+2.8}_{-22.1-3.7}$
0.0 – 0.5	$96.7 \pm 1.4^{+16.4+5.6}_{-16.3-5.7}$	$121.7 \pm 1.4^{+30.7+4.8}_{-30.7-5.0}$
0.5 – 1.0	$139.9 \pm 1.9^{+14.5+6.8}_{-14.5-7.2}$	$160.4 \pm 1.6^{+36.7+5.2}_{-36.7-5.4}$
1.0 – 1.5	$182.0 \pm 2.3^{+4.4+9.2}_{-4.4-8.6}$	$126.5 \pm 1.3^{+26.9+3.8}_{-26.9-3.7}$
1.5 – 2.0	$213.5 \pm 2.4^{+11.9+10.2}_{-11.9-9.9}$	$94.2 \pm 1.1^{+15.5+2.9}_{-15.5-3.0}$
2.0 – 2.5	$240.5 \pm 2.4^{+20.3+11.3}_{-20.3-13.2}$	$55.2 \pm 0.8^{+14.2+1.9}_{-14.2-1.9}$

Table 14: Measured differential ep cross-section $d\sigma/d\eta^{\text{jet}}$ for inclusive jet photoproduction with $E_T^{\text{jet}} > 17$ GeV. The jets have been selected according to the combination of the jet shape and subjet multiplicity into broad and narrow jets. The statistical and systematic uncertainties –not associated with the absolute energy scale of the jets– are also indicated. The systematic uncertainties associated to the absolute energy scale of the jets are quoted separately.

η^{jet}	$d\sigma/d\eta^{\text{jet}} \pm \text{stat.} \pm \text{syst.} \pm E_T^{\text{jet}} - \text{scale (pb)}$	
	broad jets	narrow jets
-1.0 – -0.5	$5.6 \pm 0.4^{+0.9+0.4}_{-0.9-0.4}$	$26.4 \pm 0.9^{+6.1+1.7}_{-6.1-1.5}$
-0.5 – 0.0	$21.1 \pm 0.7^{+0.2+1.0}_{-0.1-1.0}$	$95.4 \pm 1.5^{+7.8+3.1}_{-7.8-2.8}$
0.0 – 0.5	$41.4 \pm 1.0^{+3.9+1.9}_{-3.9-1.8}$	$181.6 \pm 2.1^{+15.8+4.2}_{-15.8-4.5}$
0.5 – 1.0	$51.4 \pm 1.1^{+5.9+1.8}_{-5.9-1.9}$	$236.1 \pm 2.5^{+14.5+4.7}_{-14.5-4.6}$
1.0 – 1.5	$57.3 \pm 1.3^{+2.7+2.1}_{-2.7-2.1}$	$252.3 \pm 2.7^{+6.3+4.7}_{-6.3-4.4}$
1.5 – 2.0	$57.5 \pm 1.1^{+3.0+2.0}_{-3.0-2.1}$	$256.3 \pm 2.6^{+9.1+5.1}_{-9.1-4.8}$
2.0 – 2.5	$49.4 \pm 1.0^{+6.1+1.8}_{-6.1-1.7}$	$211.2 \pm 2.4^{+4.0+4.3}_{-4.0-4.0}$

Table 15: Measured differential ep cross-section $d\sigma/d\eta^{\text{jet}}$ for inclusive jet production in DIS with $E_T^{\text{jet}} > 17$ GeV. The jets have been selected according to their shape into broad and narrow jets. The statistical and systematic uncertainties –not associated with the absolute energy scale of the jets– are also indicated. The systematic uncertainties associated to the absolute energy scale of the jets are quoted separately.

E_T^{jet} (GeV)	$d\sigma/dE_T^{\text{jet}} \pm \text{stat.} \pm \text{syst.} \pm E_T^{\text{jet}} - \text{scale}$ (pb)	
	broad jets	narrow jets
17. – 21.	$102.4 \pm 0.5^{+3.7+5.1}_{-3.7-5.4}$	$102.3 \pm 0.5^{+6.8+3.3}_{-6.8-3.5}$
21. – 25.	$27.2 \pm 0.3^{+1.3+1.5}_{-1.3-1.6}$	$42.7 \pm 0.3^{+2.1+1.5}_{-2.1-1.4}$
25. – 29.	$8.78 \pm 0.16^{+0.37+0.45}_{-0.37-0.53}$	$18.9 \pm 0.2^{+1.5+0.7}_{-1.5-0.8}$
29. – 35.	$3.02 \pm 0.08^{+0.26+0.22}_{-0.26-0.22}$	$7.82 \pm 0.12^{+0.43+0.41}_{-0.42-0.33}$
35. – 41.	$0.774 \pm 0.040^{+0.061+0.042}_{-0.062-0.045}$	$2.93 \pm 0.07^{+0.18+0.13}_{-0.18-0.17}$
41. – 47.	$0.231 \pm 0.022^{+0.028+0.017}_{-0.027-0.020}$	$1.094 \pm 0.046^{+0.045+0.055}_{-0.043-0.081}$
47. – 55.	$0.064 \pm 0.010^{+0.010+0.005}_{-0.010-0.003}$	$0.447 \pm 0.026^{+0.014+0.035}_{-0.014-0.033}$
55. – 71.	$0.0148 \pm 0.0036^{+0.0016+0.0013}_{-0.0016-0.0003}$	$0.068 \pm 0.006^{+0.030+0.003}_{-0.030-0.004}$
71. – 95.	$0.00050^{+0.00088+0.00098+0.00006}_{-0.00032-0.00001-0.00009}$	$0.0102 \pm 0.0027^{+0.0041+0.0000}_{-0.0039-0.0003}$

Table 16: Measured differential ep cross-section $d\sigma/dE_T^{\text{jet}}$ for inclusive jet photoproduction with $-1 < \eta^{\text{jet}} < 2.5$. The jets have been selected according to their shape into broad and narrow jets. The statistical and systematic uncertainties –not associated with the absolute energy scale of the jets– are also indicated. The systematic uncertainties associated to the absolute energy scale of the jets are quoted separately.

E_T^{jet} (GeV)	$d\sigma/dE_T^{\text{jet}} \pm \text{stat.} \pm \text{syst.} \pm E_T^{\text{jet}} - \text{scale}$ (pb)	
	broad jets	narrow jets
17. – 21.	$19.6 \pm 0.2^{+1.6+0.7}_{-1.6-0.8}$	$67.3 \pm 0.5^{+3.2+1.0}_{-3.2-1.2}$
21. – 25.	$7.76 \pm 0.15^{+0.75+0.31}_{-0.75-0.31}$	$35.2 \pm 0.3^{+1.3+0.9}_{-1.3-0.7}$
25. – 29.	$3.57 \pm 0.10^{+0.30+0.16}_{-0.30-0.13}$	$20.7 \pm 0.3^{+1.1+0.4}_{-1.1-0.3}$
29. – 35.	$1.70 \pm 0.06^{+0.04+0.07}_{-0.04-0.07}$	$10.81 \pm 0.15^{+0.67+0.28}_{-0.67-0.32}$
35. – 41.	$0.714 \pm 0.038^{+0.045+0.049}_{-0.045-0.008}$	$5.36 \pm 0.11^{+0.27+0.16}_{-0.27-0.11}$
41. – 47.	$0.312 \pm 0.026^{+0.011+0.001}_{-0.011-0.024}$	$3.02 \pm 0.08^{+0.15+0.09}_{-0.15-0.11}$
47. – 55.	$0.151 \pm 0.015^{+0.015+0.008}_{-0.015-0.003}$	$1.468 \pm 0.046^{+0.035+0.073}_{-0.035-0.052}$
55. – 71.	$0.0349 \pm 0.0052^{+0.0095+0.0018}_{-0.0095-0.0020}$	$0.572 \pm 0.021^{+0.035+0.017}_{-0.035-0.026}$
71. – 95.	$0.0099 \pm 0.0024^{+0.0017+0.0012}_{-0.0017-0.0003}$	$0.1185 \pm 0.0074^{+0.0081+0.0089}_{-0.0081-0.0055}$

Table 17: Measured differential ep cross-section $d\sigma/dE_T^{\text{jet}}$ for inclusive jet production in DIS with $-1 < \eta^{\text{jet}} < 2.5$. The jets have been selected according to their shape into broad and narrow jets. The statistical and systematic uncertainties –not associated with the absolute energy scale of the jets– are also indicated. The systematic uncertainties associated to the absolute energy scale of the jets are quoted separately.

E_T^{jet} (GeV)	$d\sigma/dE_T^{\text{jet}} \pm \text{stat.} \pm \text{syst.} \pm E_T^{\text{jet}} - \text{scale}$ (pb)	
	broad jets	narrow jets
17. – 21.	$116.6 \pm 0.6^{+1.3+5.1}_{-1.2-5.5}$	$44.7 \pm 0.3^{+13.8+1.5}_{-13.8-1.7}$
21. – 25.	$32.7 \pm 0.3^{+0.6+1.7}_{-0.6-1.7}$	$19.7 \pm 0.2^{+4.6+0.8}_{-4.6-0.7}$
25. – 29.	$10.91 \pm 0.18^{+0.17+0.58}_{-0.17-0.69}$	$9.2 \pm 0.1^{+2.4+0.3}_{-2.4-0.5}$
29. – 35.	$3.33 \pm 0.08^{+0.16+0.21}_{-0.16-0.22}$	$4.38 \pm 0.08^{+0.65+0.22}_{-0.64-0.20}$
35. – 41.	$0.868 \pm 0.040^{+0.068+0.060}_{-0.070-0.059}$	$1.74 \pm 0.05^{+0.24+0.08}_{-0.24-0.08}$
41. – 47.	$0.227 \pm 0.021^{+0.030+0.016}_{-0.030-0.018}$	$0.70 \pm 0.03^{+0.16+0.03}_{-0.16-0.05}$
47. – 55.	$0.084 \pm 0.010^{+0.016+0.008}_{-0.016-0.003}$	$0.327 \pm 0.021^{+0.015+0.028}_{-0.015-0.026}$
55. – 71.	$0.0133 \pm 0.0028^{+0.0035+0.0016}_{-0.0035-0.0007}$	$0.055 \pm 0.005^{+0.035+0.002}_{-0.035-0.003}$
71. – 95.	$0.00016^{+0.00028+0.00017+0.00000}_{-0.00010-0.00004-0.00002}$	$0.0104 \pm 0.0028^{+0.0033+0.0000}_{-0.0031-0.0004}$

Table 18: Measured differential ep cross-section $d\sigma/dE_T^{\text{jet}}$ for inclusive jet photoproduction with $-1 < \eta^{\text{jet}} < 2.5$. The jets have been selected according to their subjet multiplicity into broad and narrow jets. The statistical and systematic uncertainties –not associated with the absolute energy scale of the jets– are also indicated. The systematic uncertainties associated to the absolute energy scale of the jets are quoted separately.

E_T^{jet} (GeV)	$d\sigma/dE_T^{\text{jet}} \pm \text{stat.} \pm \text{syst.} \pm E_T^{\text{jet}} - \text{scale}$ (pb)	
	broad jets	narrow jets
17. – 21.	$82.7 \pm 0.5^{+1.1+4.1}_{-1.1-4.2}$	$40.5 \pm 0.3^{+11.1+1.3}_{-11.1-1.4}$
21. – 25.	$21.4 \pm 0.2^{+0.9+1.2}_{-0.9-1.3}$	$18.2 \pm 0.2^{+4.0+0.7}_{-4.0-0.6}$
25. – 29.	$6.72 \pm 0.14^{+0.14+0.36}_{-0.15-0.37}$	$8.7 \pm 0.1^{+2.2+0.2}_{-2.2-0.4}$
29. – 35.	$2.18 \pm 0.07^{+0.10+0.16}_{-0.10-0.17}$	$4.12 \pm 0.08^{+0.57+0.21}_{-0.57-0.18}$
35. – 41.	$0.505 \pm 0.032^{+0.062+0.023}_{-0.063-0.029}$	$1.66 \pm 0.05^{+0.20+0.08}_{-0.20-0.08}$
41. – 47.	$0.138 \pm 0.017^{+0.011+0.011}_{-0.011-0.010}$	$0.67 \pm 0.03^{+0.12+0.02}_{-0.12-0.05}$
47. – 55.	$0.044 \pm 0.008^{+0.005+0.005}_{-0.005-0.002}$	$0.317 \pm 0.021^{+0.013+0.030}_{-0.013-0.026}$
55. – 71.	$0.0071 \pm 0.0021^{+0.0012+0.0010}_{-0.0012-0.0008}$	$0.051 \pm 0.005^{+0.030+0.002}_{-0.030-0.003}$
71. – 95.		$0.0091 \pm 0.0027^{+0.0041+0.0000}_{-0.0039-0.0004}$

Table 19: Measured differential ep cross-section $d\sigma/dE_T^{\text{jet}}$ for inclusive jet photoproduction with $-1 < \eta^{\text{jet}} < 2.5$. The jets have been selected according to the combination of the jet shape and subjet multiplicity into broad and narrow jets. The statistical and systematic uncertainties –not associated with the absolute energy scale of the jets– are also indicated. The systematic uncertainties associated to the absolute energy scale of the jets are quoted separately.

$ \cos\theta^* $	$d\sigma/d \cos\theta^* \pm \text{stat.} \pm \text{syst.} \pm E_T^{\text{jet}} - \text{scale (pb)}$	
	broad-broad dijets	narrow-narrow dijets
0.0 – 0.2	$3.93 \pm 0.49^{+0.22+0.33}_{-0.22-0.35}$	$43.9 \pm 1.6^{+3.7+1.9}_{-3.7-1.6}$
0.2 – 0.4	$7.3 \pm 0.7^{+1.4+0.5}_{-1.4-0.4}$	$49.0 \pm 1.7^{+4.3+1.9}_{-4.2-2.1}$
0.4 – 0.6	$10.4 \pm 0.8^{+1.1+0.5}_{-1.1-1.1}$	$67.9 \pm 2.0^{+7.3+2.3}_{-7.3-3.0}$
0.6 – 0.8	$29.9 \pm 1.2^{+3.2+2.0}_{-3.2-1.6}$	$86.3 \pm 2.3^{+5.4+3.0}_{-5.4-3.6}$

Table 20: Measured differential ep cross-section $d\sigma/d|\cos\theta^*|$ for dijet photo-production with $M^{\text{jj}} > 52$ GeV. The events have been selected according to their shape into broad-broad and narrow-narrow dijets. The statistical and systematic uncertainties –not associated with the absolute energy scale of the jets– are also indicated. The systematic uncertainties associated to the absolute energy scale of the jets are quoted separately.

$\cos\theta_{\text{broad}}^*$	$d\sigma/d\cos\theta_{\text{broad}}^* \pm \text{stat.} \pm \text{syst.} \pm E_T^{\text{jet}} - \text{scale (pb)}$
	broad-narrow dijets
–0.8 – –0.6	$30.3 \pm 1.2^{+4.2+1.4}_{-4.2-1.5}$
–0.6 – –0.4	$16.5 \pm 0.9^{+2.6+0.8}_{-2.6-0.9}$
–0.4 – –0.2	$14.5 \pm 0.9^{+2.0+0.6}_{-2.0-0.4}$
–0.2 – 0.0	$10.3 \pm 0.7^{+1.8+0.5}_{-1.8-0.7}$
0.0 – 0.2	$12.8 \pm 0.8^{+1.7+0.8}_{-1.7-0.5}$
0.2 – 0.4	$17.0 \pm 1.0^{+2.3+0.7}_{-2.3-1.0}$
0.4 – 0.6	$31.7 \pm 1.4^{+1.6+1.5}_{-1.6-1.7}$
0.6 – 0.8	$66.4 \pm 1.9^{+9.3+2.9}_{-9.3-3.6}$

Table 21: Measured differential ep cross-section $d\sigma/d\cos\theta_{\text{broad}}^*$ for dijet photo-production with $M^{\text{jj}} > 52$ GeV. The events have been selected according to their shape into broad-narrow dijets. The statistical and systematic uncertainties –not associated with the absolute energy scale of the jets– are also indicated. The systematic uncertainties associated to the absolute energy scale of the jets are quoted separately.

M^{jj} (GeV)	$d\sigma/dM^{\text{jj}} \pm \text{stat.} \pm \text{syst.} \pm E_T^{\text{jet}} - \text{scale}$ (pb)	
	broad-broad dijets	narrow-narrow dijets
52. – 57.	$1.006 \pm 0.047^{+0.038+0.060}_{-0.036-0.057}$	$3.06 \pm 0.08^{+0.47+0.11}_{-0.47-0.15}$
57. – 65.	$0.387 \pm 0.022^{+0.035+0.030}_{-0.035-0.030}$	$1.842 \pm 0.053^{+0.088+0.049}_{-0.088-0.051}$
65. – 83.	$0.105 \pm 0.008^{+0.004+0.004}_{-0.004-0.006}$	$0.749 \pm 0.022^{+0.078+0.032}_{-0.078-0.031}$
83. – 103.	$0.0109 \pm 0.0023^{+0.0015+0.0015}_{-0.0015-0.0011}$	$0.210 \pm 0.011^{+0.005+0.011}_{-0.005-0.008}$
103. – 123.	$0.0015^{+0.0012+0.0016+0.0003}_{-0.0010-0.0003-0.0001}$	$0.0574 \pm 0.0059^{+0.0052+0.0026}_{-0.0053-0.0074}$

Table 22: Measured differential ep cross-section $d\sigma/dM^{\text{jj}}$ for dijet photoproduction with $|\cos\theta^*| < 0.8$. The events have been selected according to their shape into broad-broad and narrow-narrow dijets. The statistical and systematic uncertainties –not associated with the absolute energy scale of the jets– are also indicated. The systematic uncertainties associated to the absolute energy scale of the jets are quoted separately.

x_γ^{obs}	$d\sigma/dx_\gamma^{\text{obs}} \pm \text{stat.} \pm \text{syst.} \pm E_T^{\text{jet}} - \text{scale}$ (pb)	
	broad-broad dijets	narrow-narrow dijets
0.0 – 0.2	$31.6 \pm 1.5^{+1.7+2.2}_{-1.8-1.6}$	$9.0 \pm 0.8^{+0.9+0.3}_{-0.8-0.3}$
0.2 – 0.4	$79.2 \pm 2.3^{+4.7+4.0}_{-4.6-4.8}$	$48.7 \pm 1.7^{+5.1+0.3}_{-5.3-1.5}$
0.4 – 0.6	$66.0 \pm 2.0^{+1.8+2.5}_{-1.8-2.6}$	$78.1 \pm 2.2^{+4.3+0.8}_{-4.4-1.1}$
0.6 – 0.8	$71.9 \pm 2.0^{+11.2+2.6}_{-11.1-2.5}$	$131.1 \pm 2.8^{+12.4+0.2}_{-12.0-1.3}$
0.8 – 1.0	$79.0 \pm 1.9^{+20.6+7.0}_{-20.3-8.9}$	$459.6 \pm 5.4^{+58.5+19.2}_{-58.1-20.3}$

Table 23: Measured differential ep cross-section $d\sigma/dx_\gamma^{\text{obs}}$ for dijet photoproduction. The events have been selected according to their shape into broad-broad and narrow-narrow dijets. The statistical and systematic uncertainties –not associated with the absolute energy scale of the jets– are also indicated. The systematic uncertainties associated to the absolute energy scale of the jets are quoted separately.

$\langle E_T^{\text{jet}} \rangle$ (GeV)	$\alpha_s(M_Z) \pm \text{stat.} \pm \text{syst.} \pm \text{th.}$
22.9	$0.1177 \pm 0.0013^{+0.0005+0.0096}_{-0.0027-0.0076}$
26.8	$0.1177 \pm 0.0018^{+0.0018+0.0092}_{-0.0036-0.0073}$
31.6	$0.1179 \pm 0.0021^{+0.0021+0.0089}_{-0.0013-0.0071}$
37.7	$0.1188 \pm 0.0032^{+0.0010+0.0091}_{-0.0044-0.0074}$
43.7	$0.1134 \pm 0.0045^{+0.0067+0.0077}_{-0.0046-0.0061}$
50.5	$0.1165 \pm 0.0058^{+0.0001+0.0084}_{-0.0061-0.0070}$
58.5	$0.1126 \pm 0.0068^{+0.0165+0.0075}_{-0.0053-0.0062}$
79.3	$0.120 \pm 0.014^{+0.004+0.009}_{-0.013-0.008}$

Table 24: The $\alpha_s(M_Z)$ values determined from the QCD fit of the measured $\langle \psi(r = 0.5) \rangle$ as a function of E_T^{jet} in DIS. The statistical, systematic and theoretical uncertainties are also indicated.

ZEUS

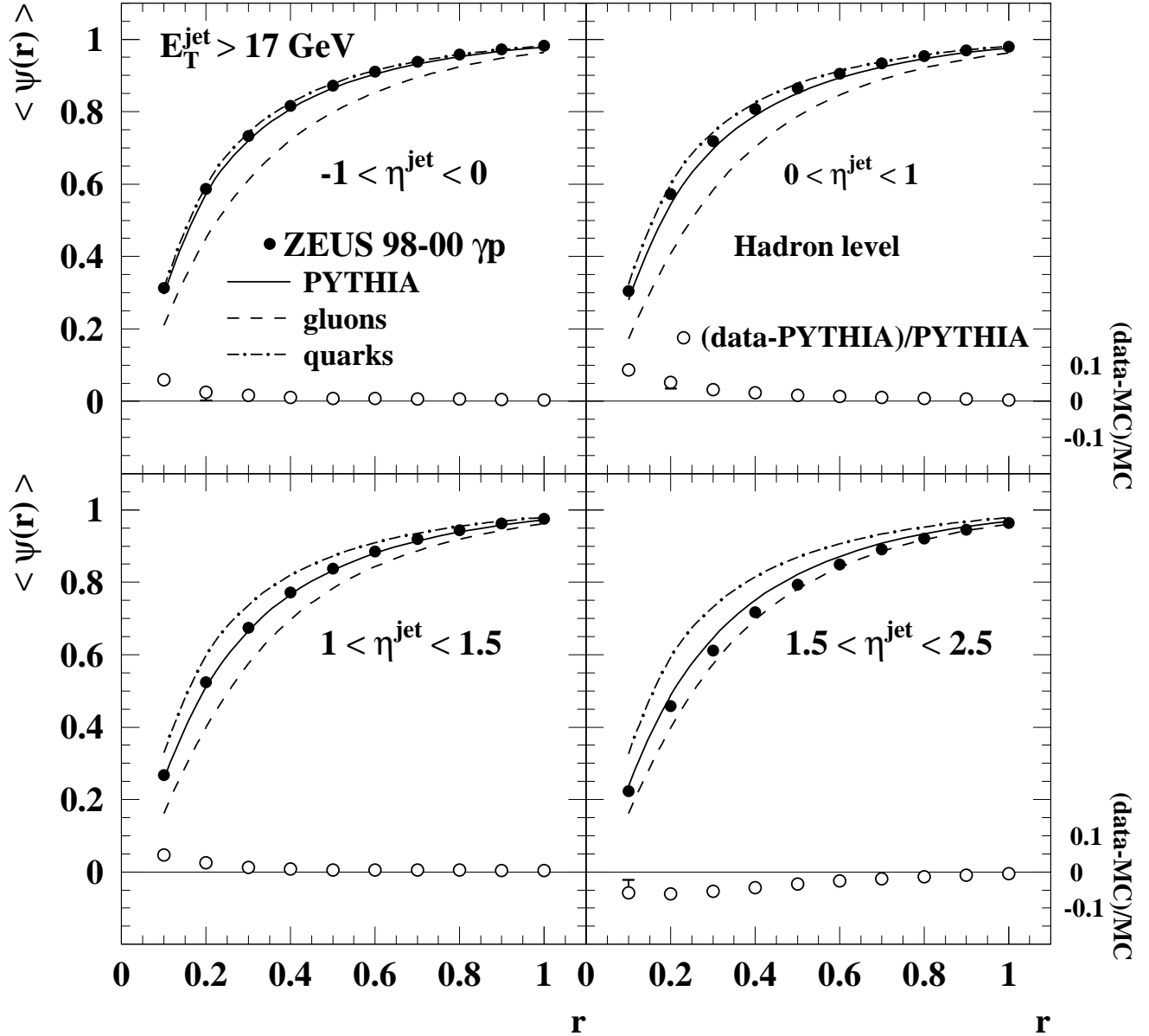


Figure 1: Measured mean integrated jet shape corrected to the hadron level (dots), $\langle \psi(r) \rangle$, for jets in photoproduction with $E_T^{\text{jet}} > 17 \text{ GeV}$ in different η^{jet} regions. The error bars, which are typically smaller than the dots, show the statistical and systematic uncertainties added in quadrature. For comparison, the predictions of PYTHIA including resolved plus direct processes for quark (dot-dashed lines), gluon (dashed lines) and all (solid lines) jets are shown. The open circles show the fractional difference of the data to the predictions of PYTHIA for all jets.

ZEUS

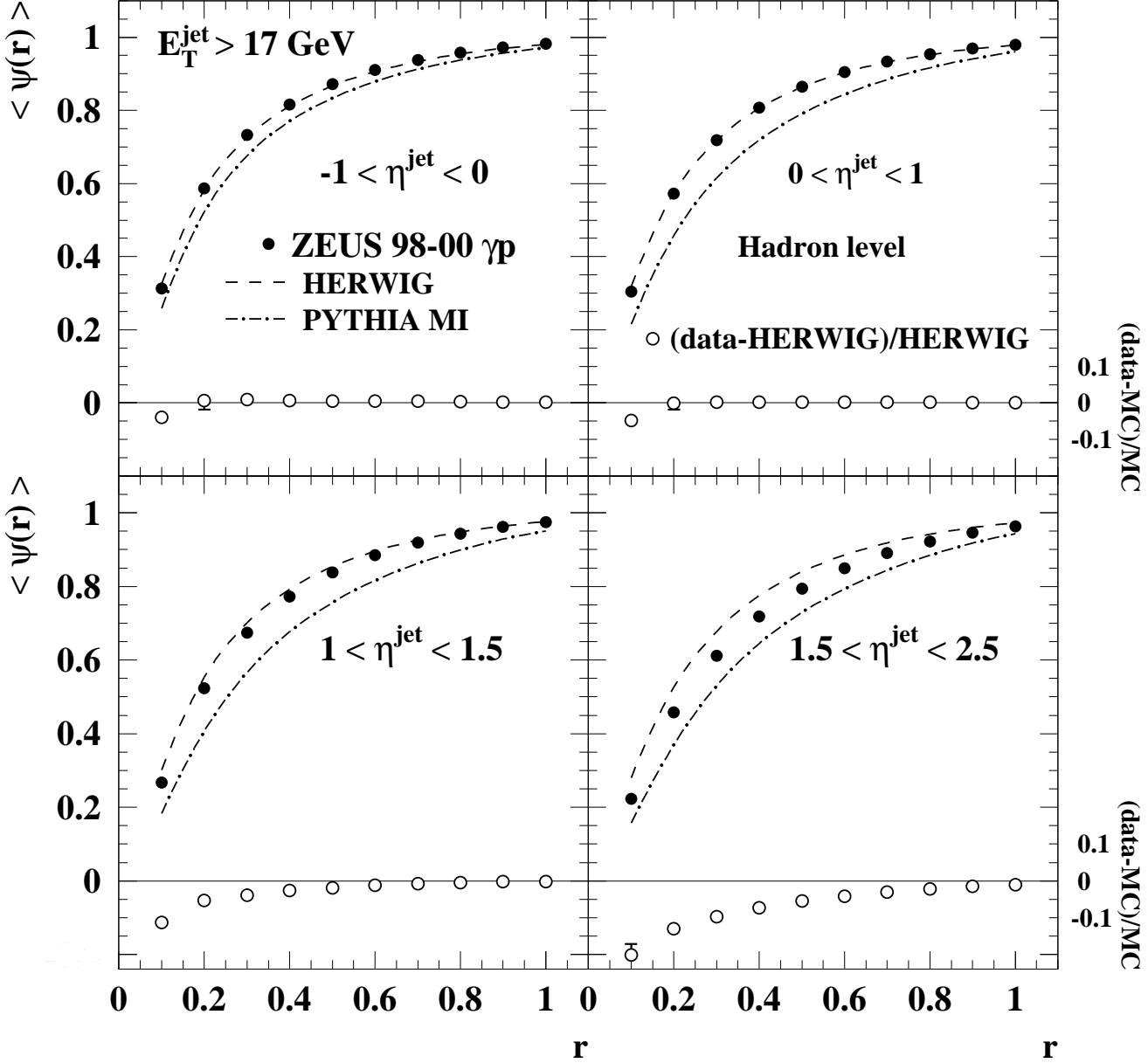


Figure 2: Measured mean integrated jet shape corrected to the hadron level (dots), $\langle \psi(r) \rangle$, for jets in photoproduction with $E_T^{\text{jet}} > 17 \text{ GeV}$ in different η^{jet} regions. For comparison, the predictions of HERWIG (dashed lines) and PYTHIA MI (dot-dashed lines) including resolved plus direct processes are shown. The open circles show the fractional difference of the data to the predictions of HERWIG. Other details are as in the caption to Fig. 1.

ZEUS

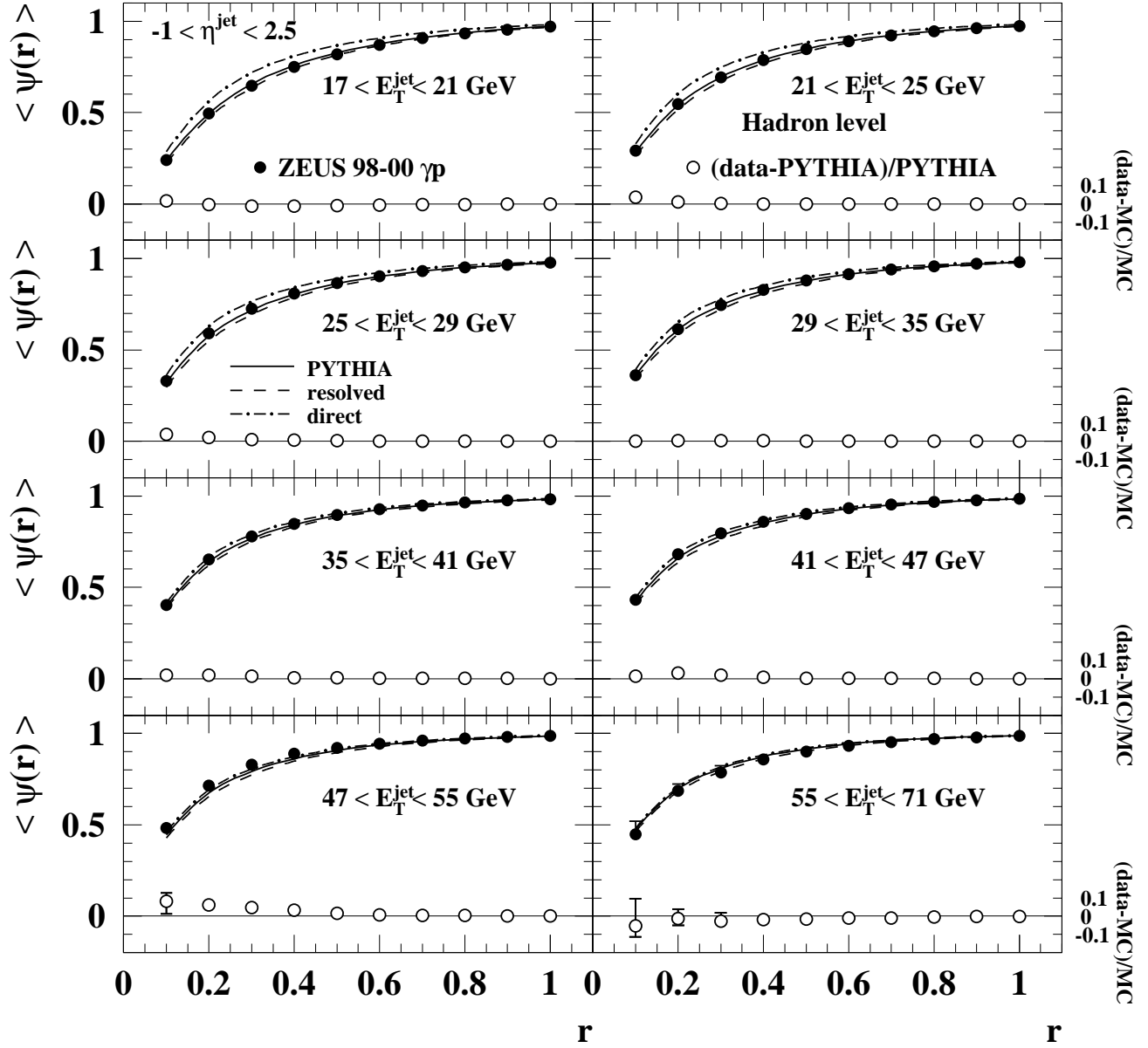


Figure 3: Measured mean integrated jet shape corrected to the hadron level (dots), $\langle \psi(r) \rangle$, for jets in photoproduction in the range $-1 < \eta^{\text{jet}} < 2.5$ in different E_T^{jet} regions. For comparison, the predictions of PYTHIA including resolved (dashed lines), direct (dot-dashed lines) and resolved plus direct processes (solid lines) are shown. Other details are as in the caption to Fig. 1.

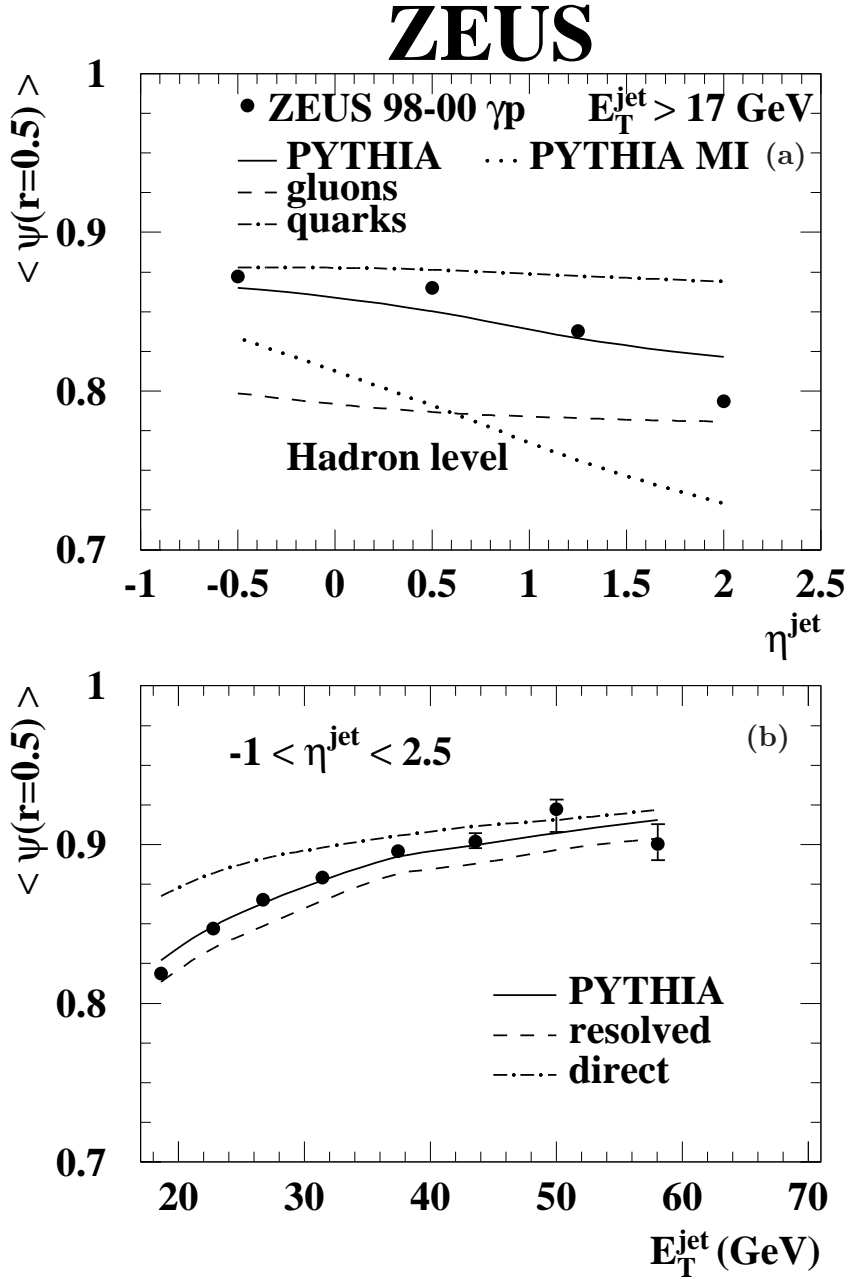


Figure 4: Measured mean integrated jet shape in photoproduction corrected to the hadron level at a fixed value of $r = 0.5$ (dots), $\langle \psi(r = 0.5) \rangle$, as a function of (a) η^{jet} with $E_T^{\text{jet}} > 17 \text{ GeV}$ and (b) E_T^{jet} with $-1 < \eta^{\text{jet}} < 2.5$. Other details are as in the captions to Figs. 1 and 3.

ZEUS

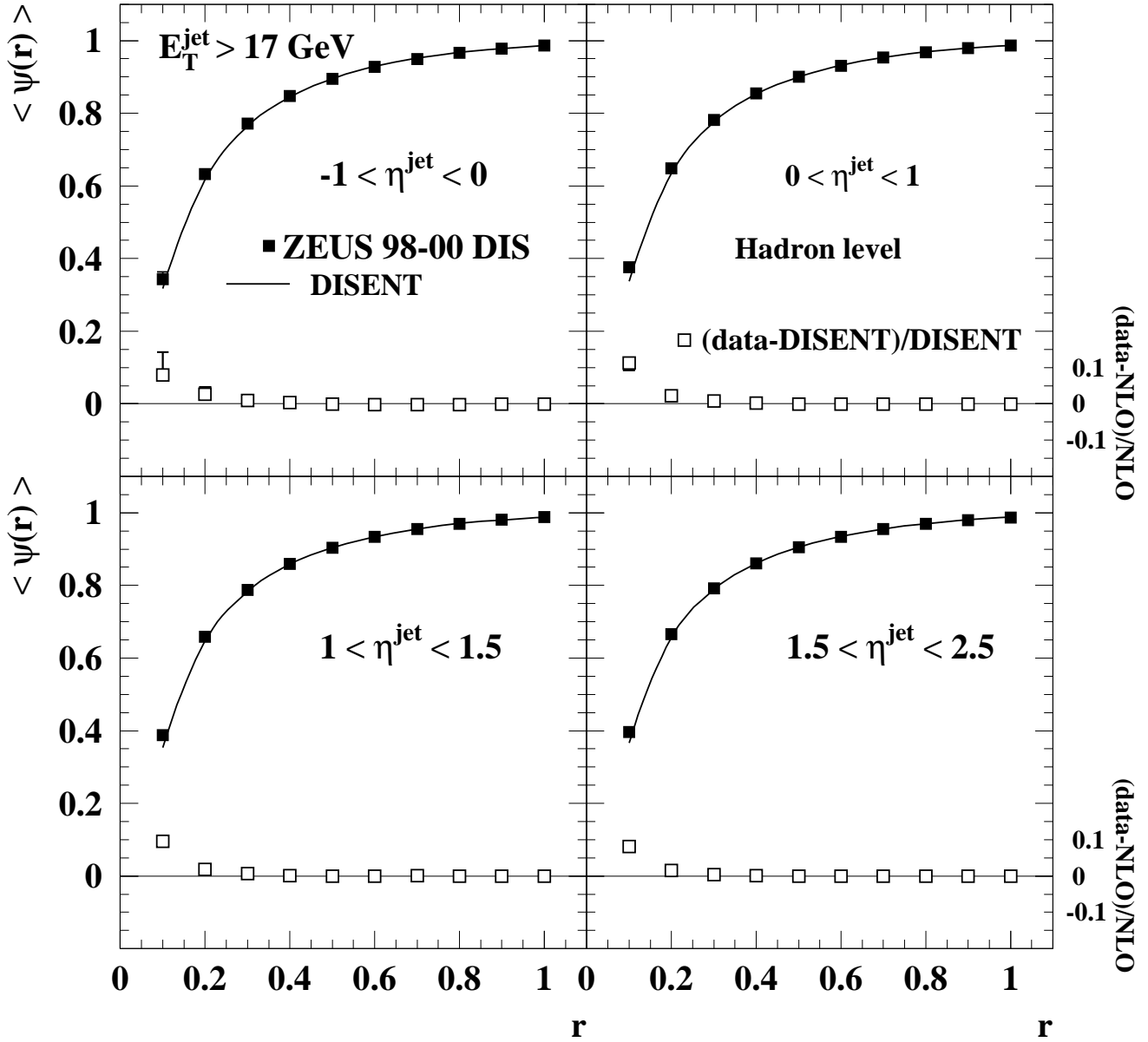


Figure 5: Measured mean integrated jet shape corrected to the hadron level and for electroweak radiative effects (squares), $\langle \psi(r) \rangle$, for jets in DIS with $E_T^{\text{jet}} > 17 \text{ GeV}$ in different η^{jet} regions. For comparison, NLO predictions corrected for hadronisation and Z^0 -exchange effects (solid lines) are shown. Other details are as in the caption to Fig. 1.

ZEUS

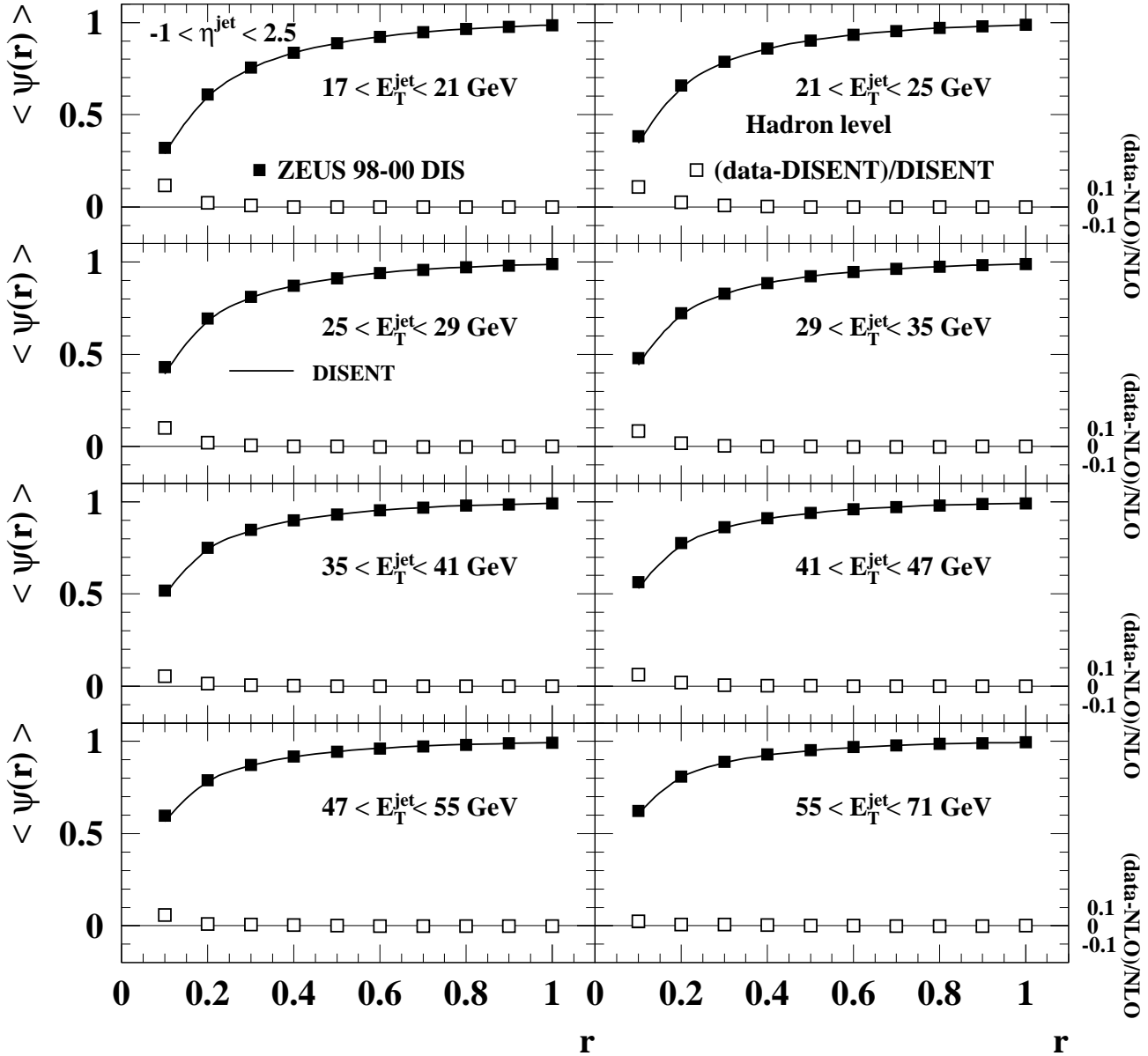


Figure 6: Measured mean integrated jet shape corrected to the hadron level and for electroweak radiative effects (squares), $\langle \psi(r) \rangle$, for jets in DIS in the range $-1 < \eta^{\text{jet}} < 2.5$ in different E_T^{jet} regions. Other details are as in the captions to Figs. 1 and 5.

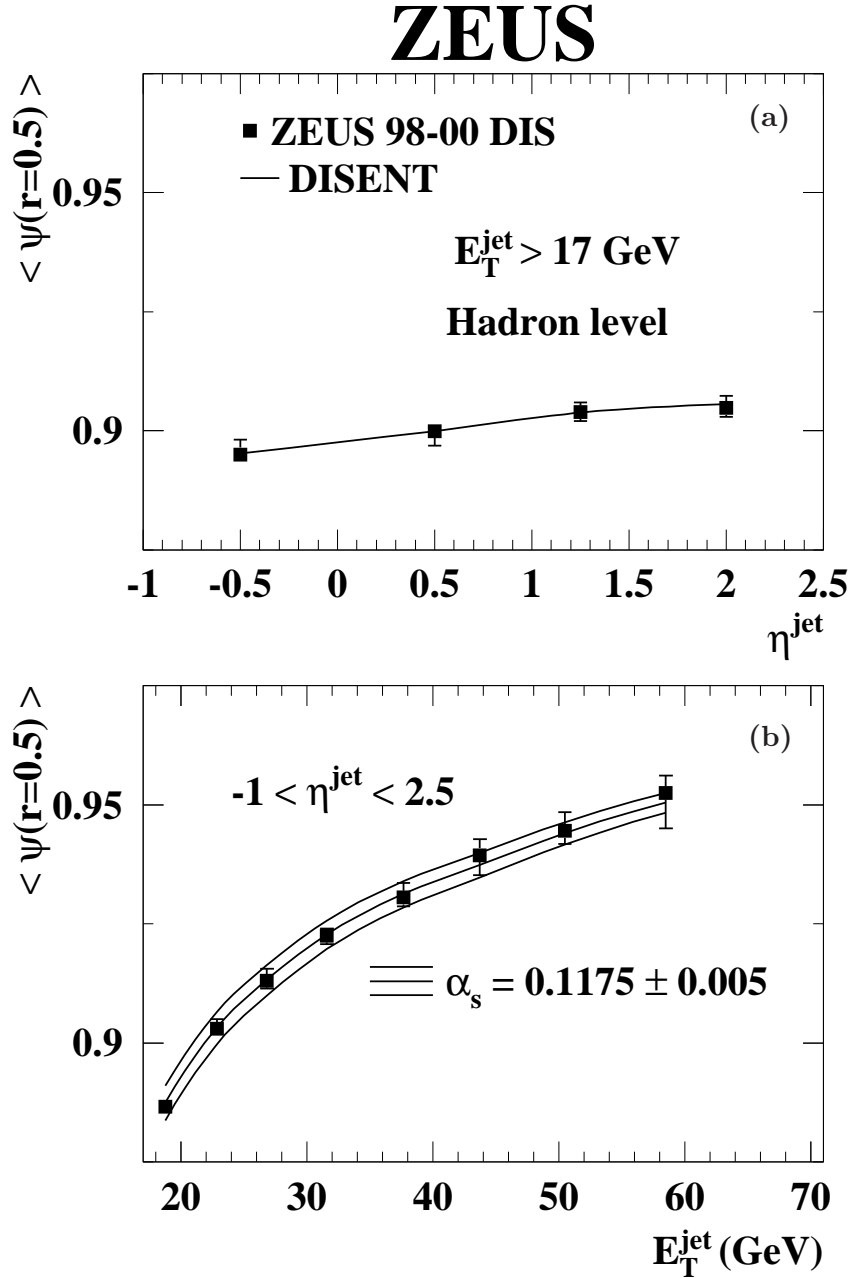


Figure 7: Measured mean integrated jet shape in DIS corrected to the hadron level and for electroweak radiative effects at a fixed value of $r = 0.5$ (squares), $\langle \psi(r = 0.5) \rangle$, as a function of (a) η^{jet} with $E_T^{\text{jet}} > 17 \text{ GeV}$ and (b) E_T^{jet} with $-1 < \eta^{\text{jet}} < 2.5$. Other details are as in the caption to Fig. 5.

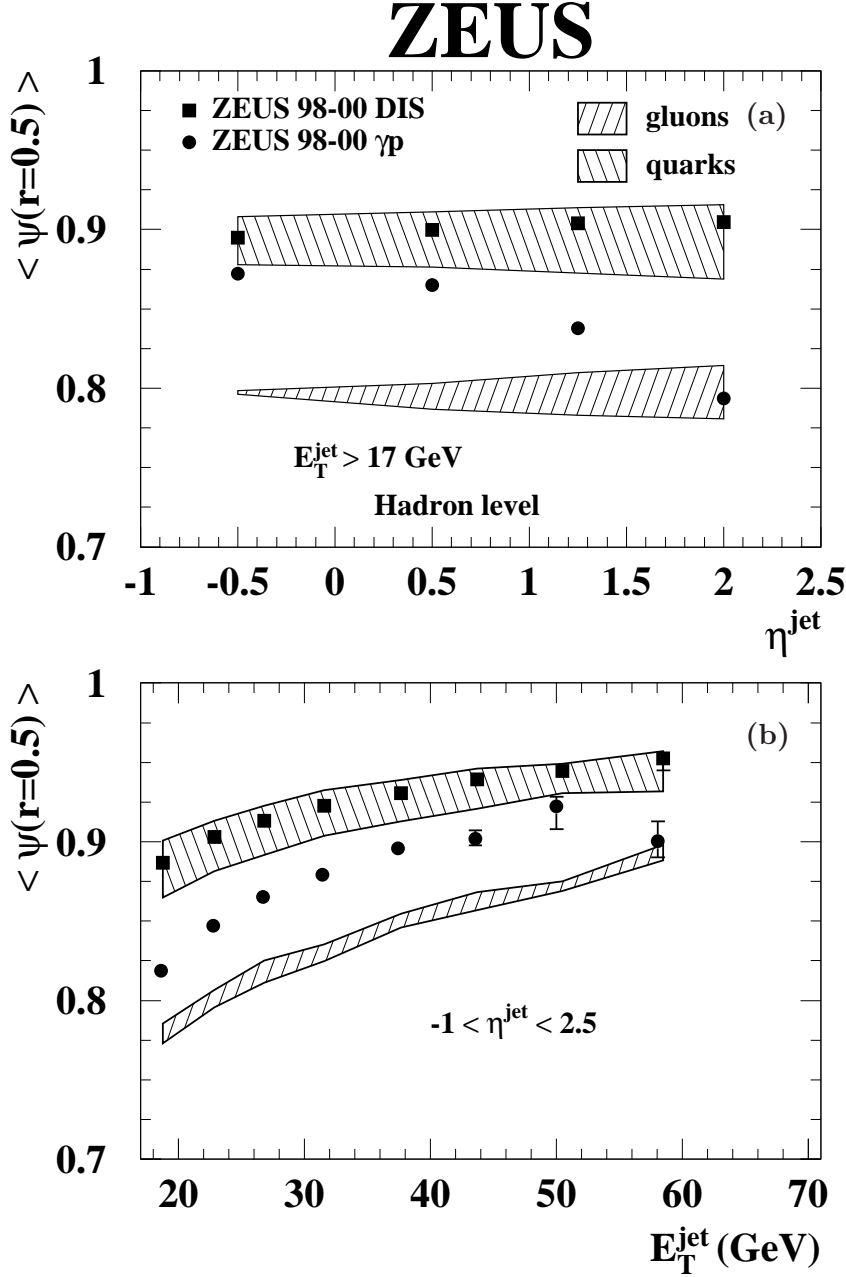


Figure 8: Measured mean integrated jet shape corrected to the hadron level at a fixed value of $r = 0.5$ for DIS (squares) and photoproduction (dots), $\langle \psi(r = 0.5) \rangle$, as a function of (a) η^{jet} with $E_T^{\text{jet}} > 17 \text{ GeV}$ and (b) E_T^{jet} with $-1 < \eta^{\text{jet}} < 2.5$. The predictions for gluon-initiated (lower hatched areas) and quark-initiated (upper hatched areas) jets are also shown. The bounds of each hatched area are given by the predictions of CDM and PYTHIA. Other details are as in the caption to Fig. 5.

ZEUS

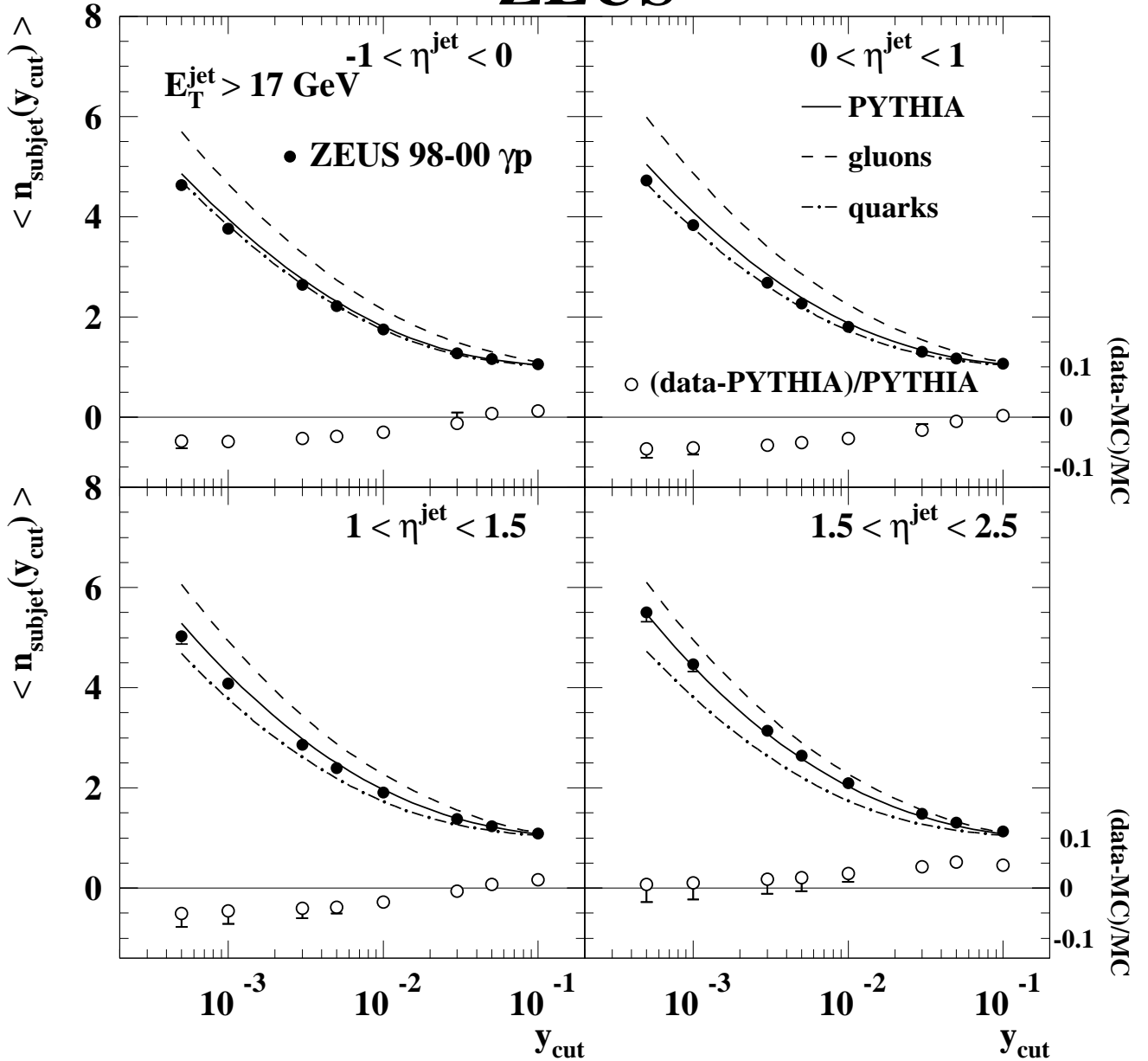


Figure 9: Measured mean subjet multiplicity corrected to the hadron level (dots), $\langle n_{\text{subjet}}(y_{\text{cut}}) \rangle$, for jets in photoproduction with $E_T^{\text{jet}} > 17 \text{ GeV}$ in different η^{jet} regions. Other details are as in the caption to Fig. 1.

ZEUS

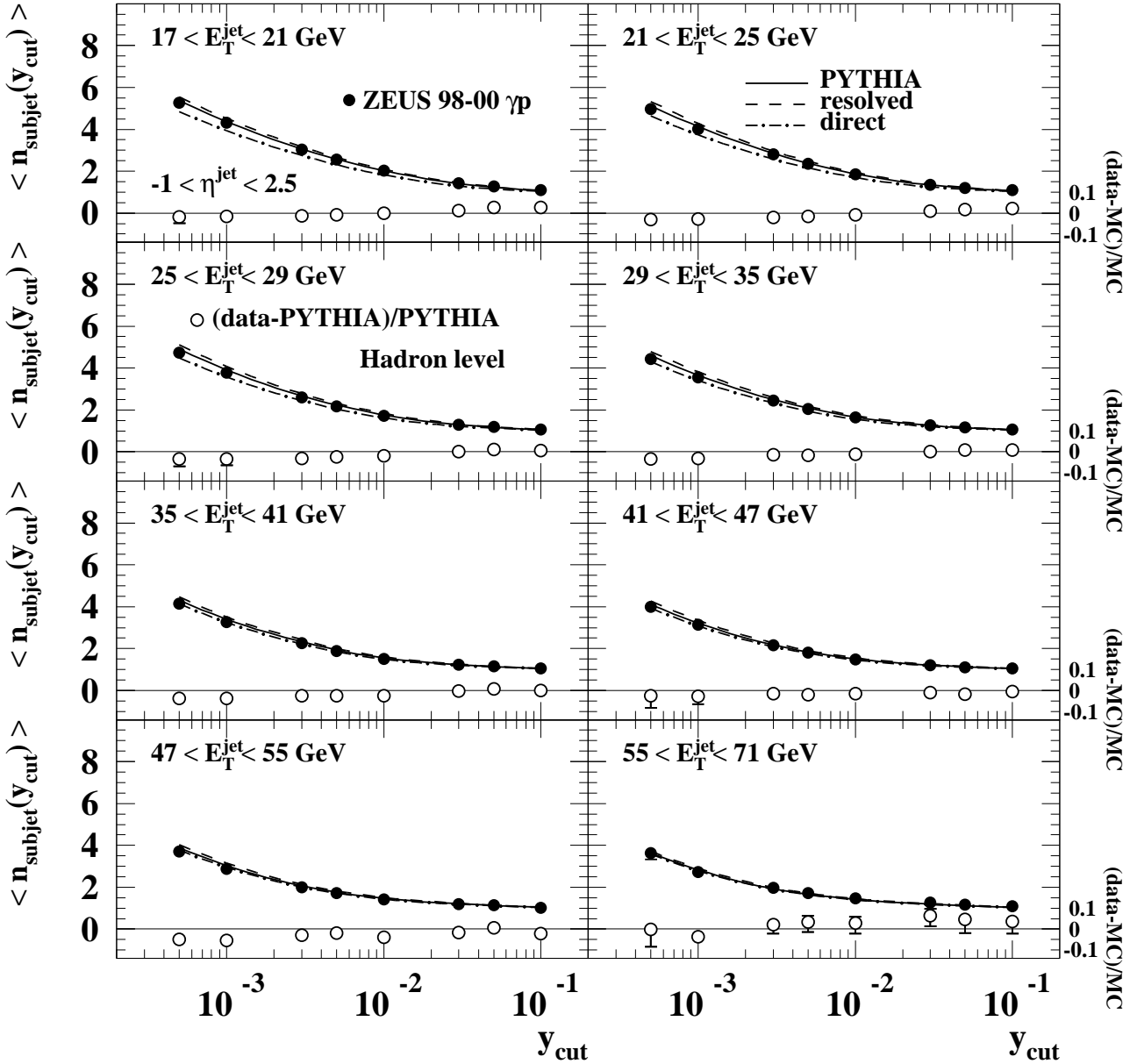


Figure 10: Measured mean subjet multiplicity corrected to the hadron level (dots), $\langle n_{\text{subjet}}(y_{\text{cut}}) \rangle$, for jets in photoproduction in the range $-1 < \eta^{\text{jet}} < 2.5$ in different E_T^{jet} regions. Other details are as in the caption to Fig. 3.

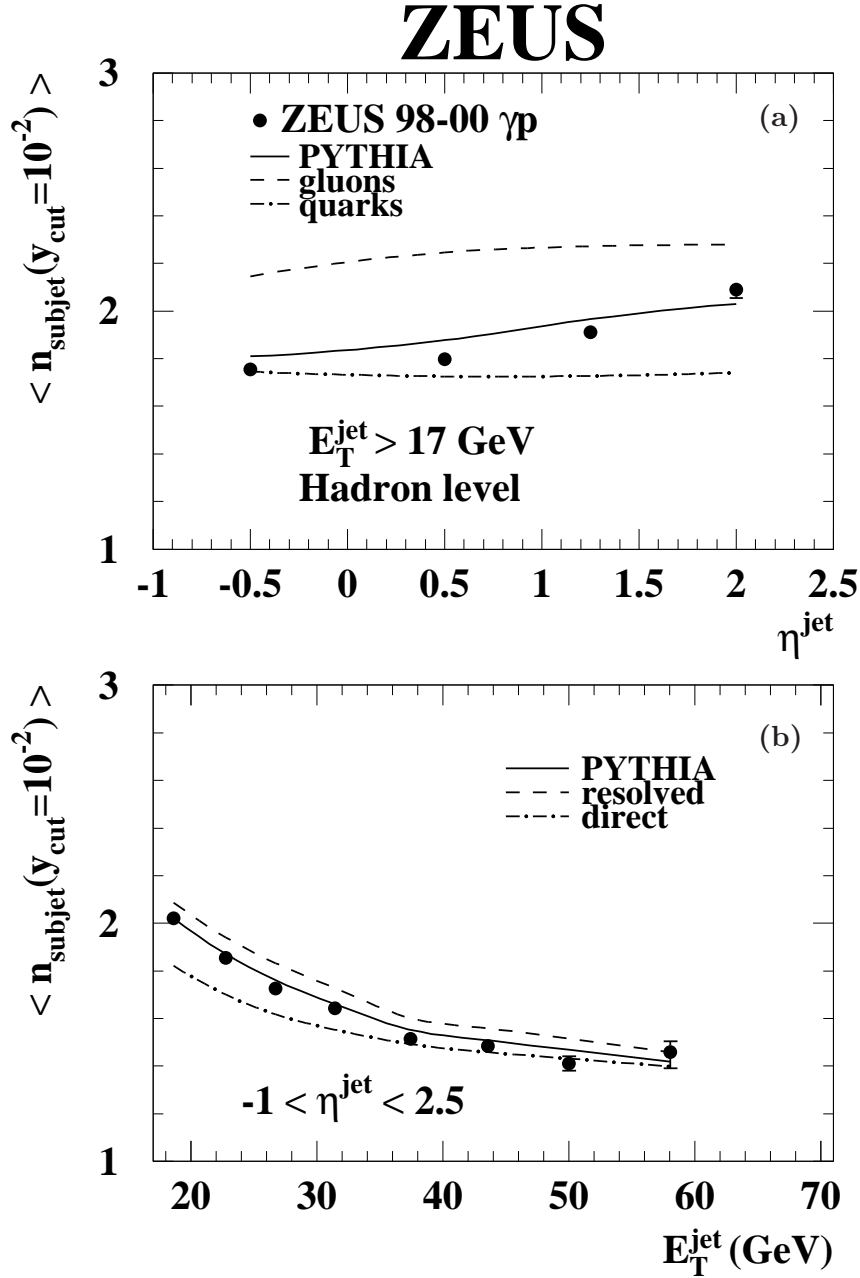


Figure 11: Measured mean subjet multiplicity in photoproduction corrected to the hadron level at a fixed value of $y_{\text{cut}} = 10^{-2}$ (dots), $\langle n_{\text{subjet}}(y_{\text{cut}} = 10^{-2}) \rangle$, as a function of (a) η^{jet} with $E_T^{\text{jet}} > 17 \text{ GeV}$ and (b) E_T^{jet} with $-1 < \eta^{\text{jet}} < 2.5$. Other details are as in the caption to Fig. 4.

ZEUS

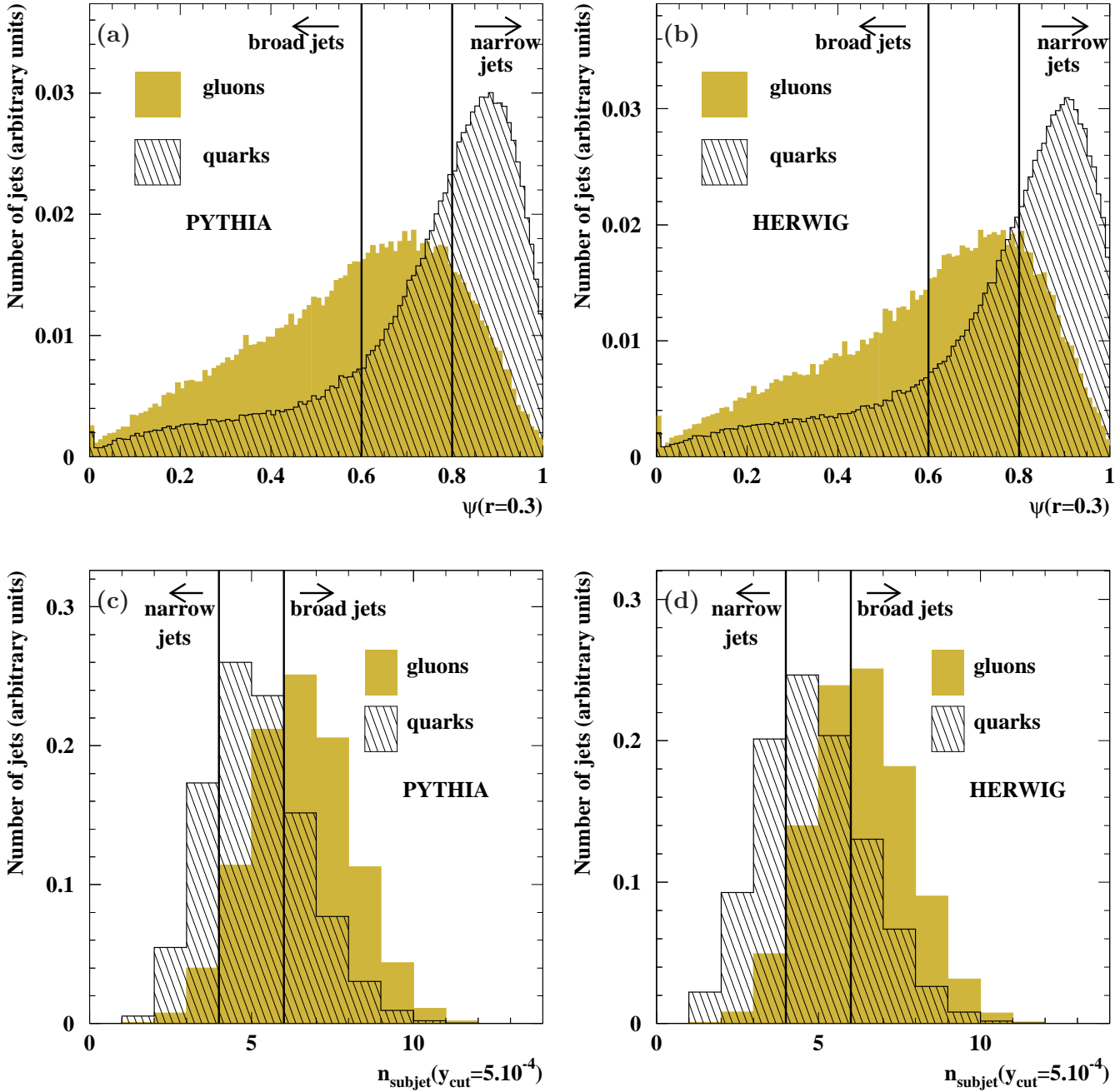


Figure 12: (a) The predicted integrated jet shape distribution at $r = 0.3$ and (c) the predicted subjet multiplicity distribution at $y_{\text{cut}} = 5 \cdot 10^{-4}$ at the hadron level for samples of gluon- (shaded histograms) and quark-initiated (hatched histograms) jets simulated using the program PYTHIA; (b) and (d) show the same distributions for samples of HERWIG.

ZEUS

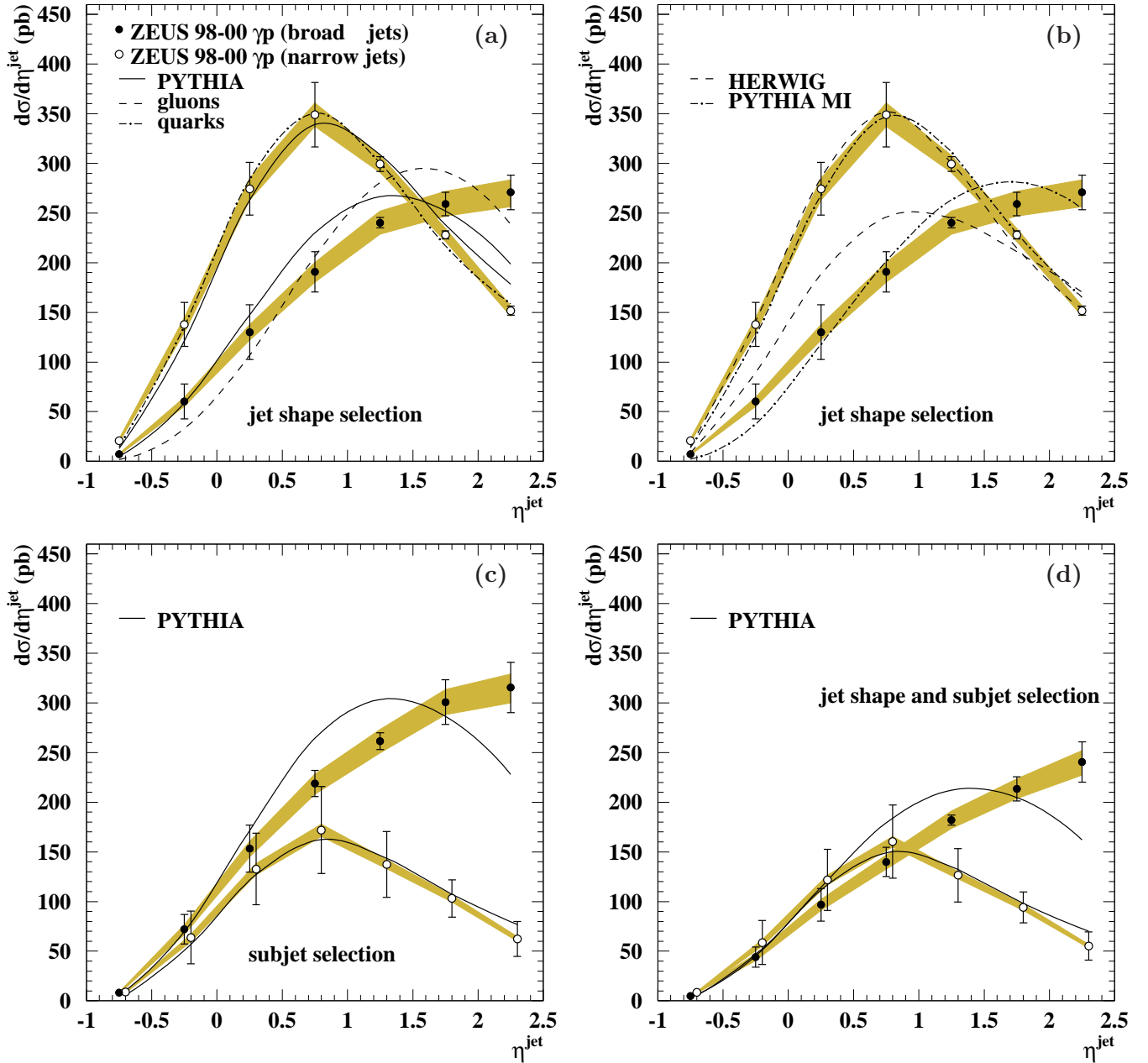


Figure 13: Measured differential ep cross-section $d\sigma/d\eta^{\text{jet}}$ for inclusive jet photoproduction with $E_T^{\text{jet}} > 17$ GeV in the kinematic region defined by $Q^2 < 1$ GeV² and $142 < W_{\gamma p} < 293$ GeV. The jets have been selected according to (a,b) their shape, (c) subjet multiplicity or (d) a combination of both in broad jets (dots) and narrow jets (open circles). The thick error bars (not visible) represent the statistical uncertainties of the data, and the thin error bars show the statistical and systematic uncertainties –not associated with the uncertainty in the absolute energy scale of the jets, shown as a shaded band– added in quadrature. The calculations of PYTHIA for resolved plus direct processes separated according to the same criteria as in the data are included in (a,c,d) (solid lines). In (a), the calculations of PYTHIA for gluon (dashed line) and quark (dot-dashed line) jets are also included. In (b), the calculations of HERWIG (dashed lines) and PYTHIA MI (dot-dashed lines) with the same selection as in the data are included. The MC calculations have been normalised to the total measured cross section of each type. In (c) and (d), the measurements and predictions for narrow jets have been plotted at $\eta^{\text{jet}} + 0.05$ for clarity of presentation.

ZEUS

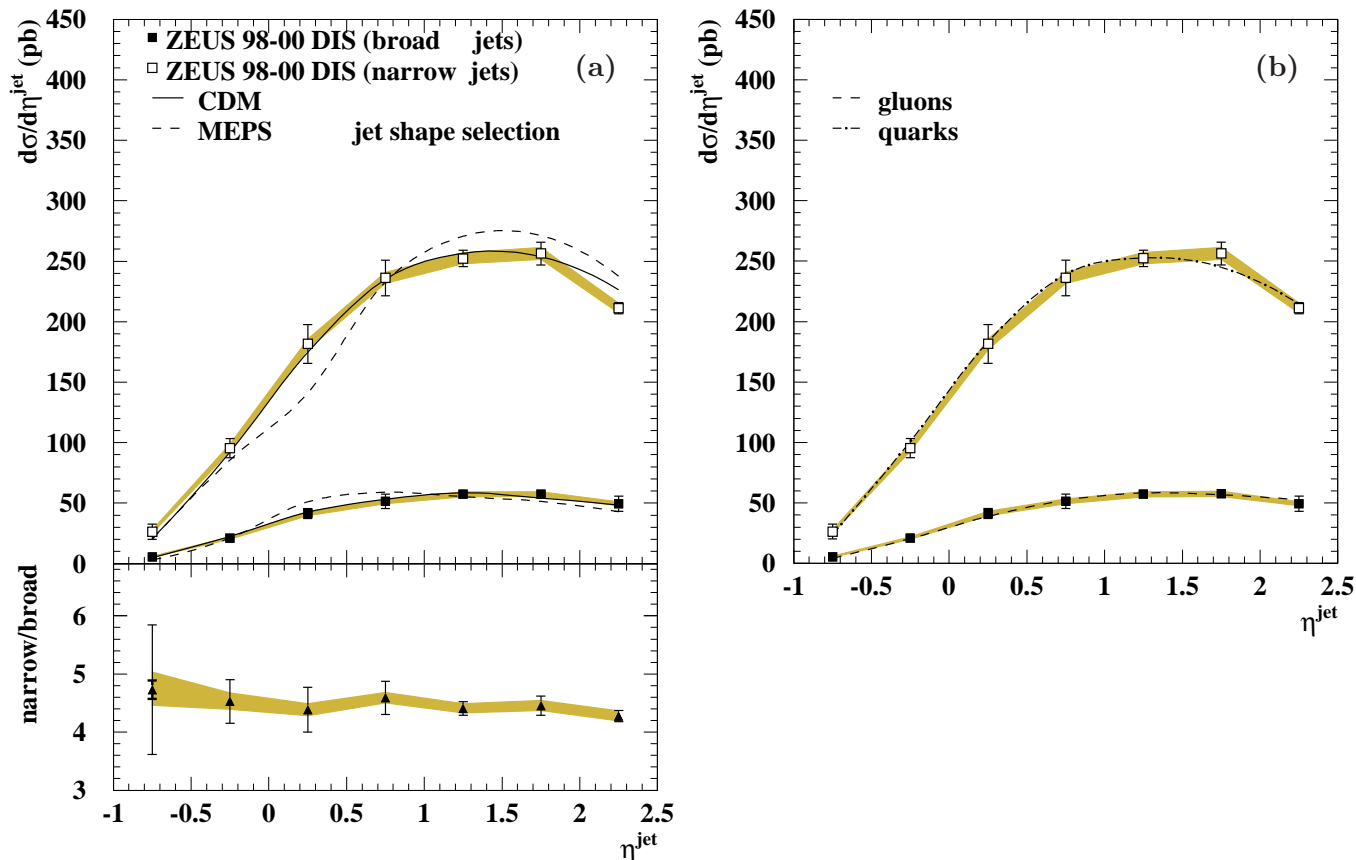


Figure 14: Measured differential ep cross-section $d\sigma/d\eta^{\text{jet}}$ for inclusive jets in DIS with $E_T^{\text{jet}} > 17$ GeV in the kinematic region defined by $Q^2 > 125$ GeV². The jets have been selected according to their shape as broad jets (black squares) and narrow jets (white squares). The lower part of (a) shows the ratio between the measured $d\sigma/d\eta^{\text{jet}}$ for the narrow- and broad-jet samples (triangles). The calculations of CDM (solid lines) and MEPS (dashed lines) are included in (a). In (b), the calculations of CDM for gluon- (dashed line) and quark-initiated (dot-dashed line) jets are included. Other details are as in the caption to Fig. 13.

ZEUS

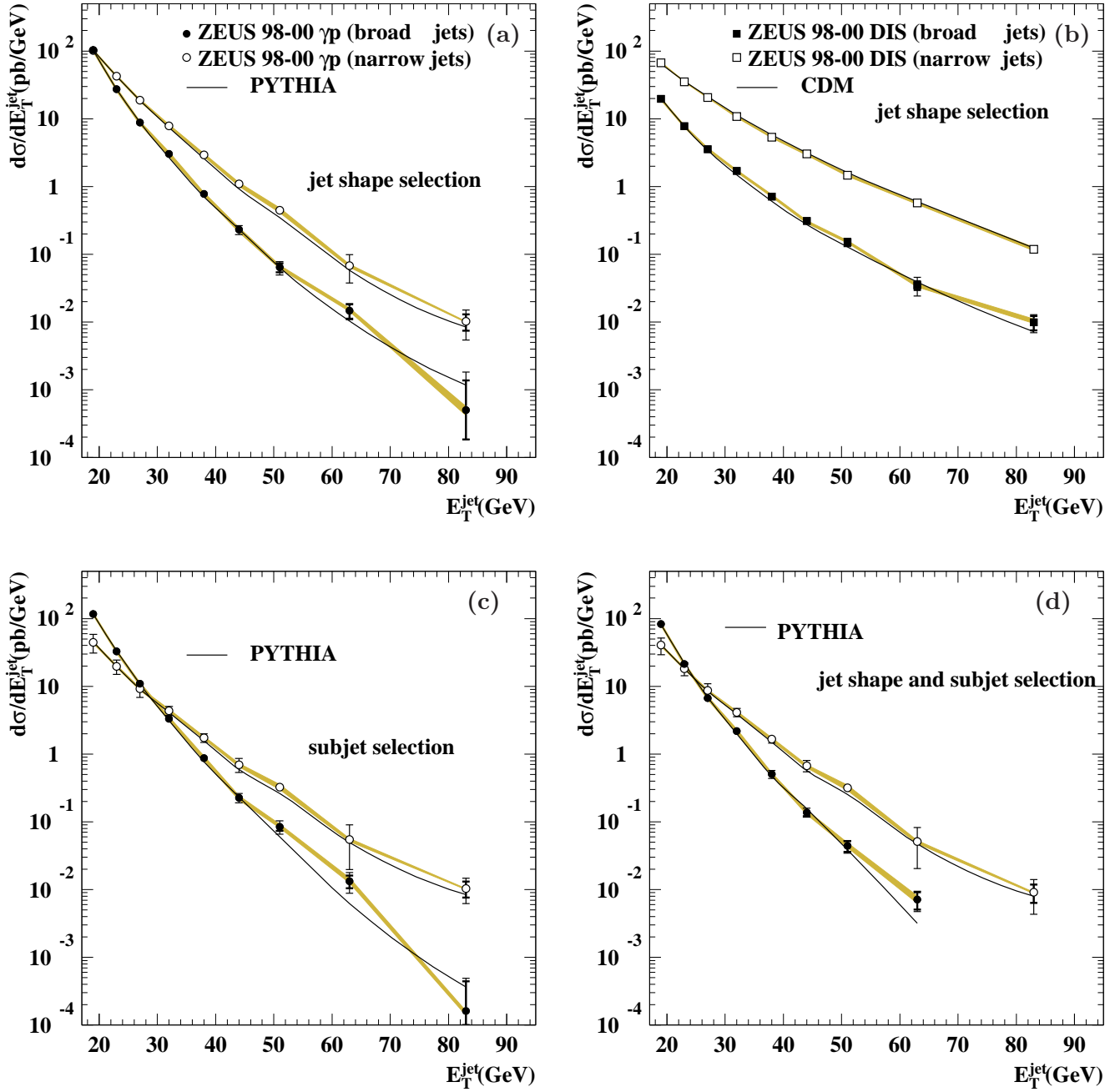


Figure 15: (a) Measured differential ep cross-section $d\sigma/dE_T^{\text{jet}}$ for inclusive jet photoproduction in the range $-1 < \eta^{\text{jet}} < 2.5$ in the kinematic region defined by $Q^2 < 1 \text{ GeV}^2$ and $142 < W_{\gamma p} < 293 \text{ GeV}$. (b) Measured differential ep cross-section $d\sigma/dE_T^{\text{jet}}$ for inclusive jet DIS in the range $-1 < \eta^{\text{jet}} < 2.5$ in the kinematic region defined by $Q^2 > 125 \text{ GeV}^2$. In (a) and (b), the jets have been selected according to their shape. In (c) and (d), the photoproduced jets have been selected according to the subjet multiplicity and the combination of jet shape and subjet multiplicity, respectively. Other details are as in the captions to Figs. 13 and 14.

ZEUS

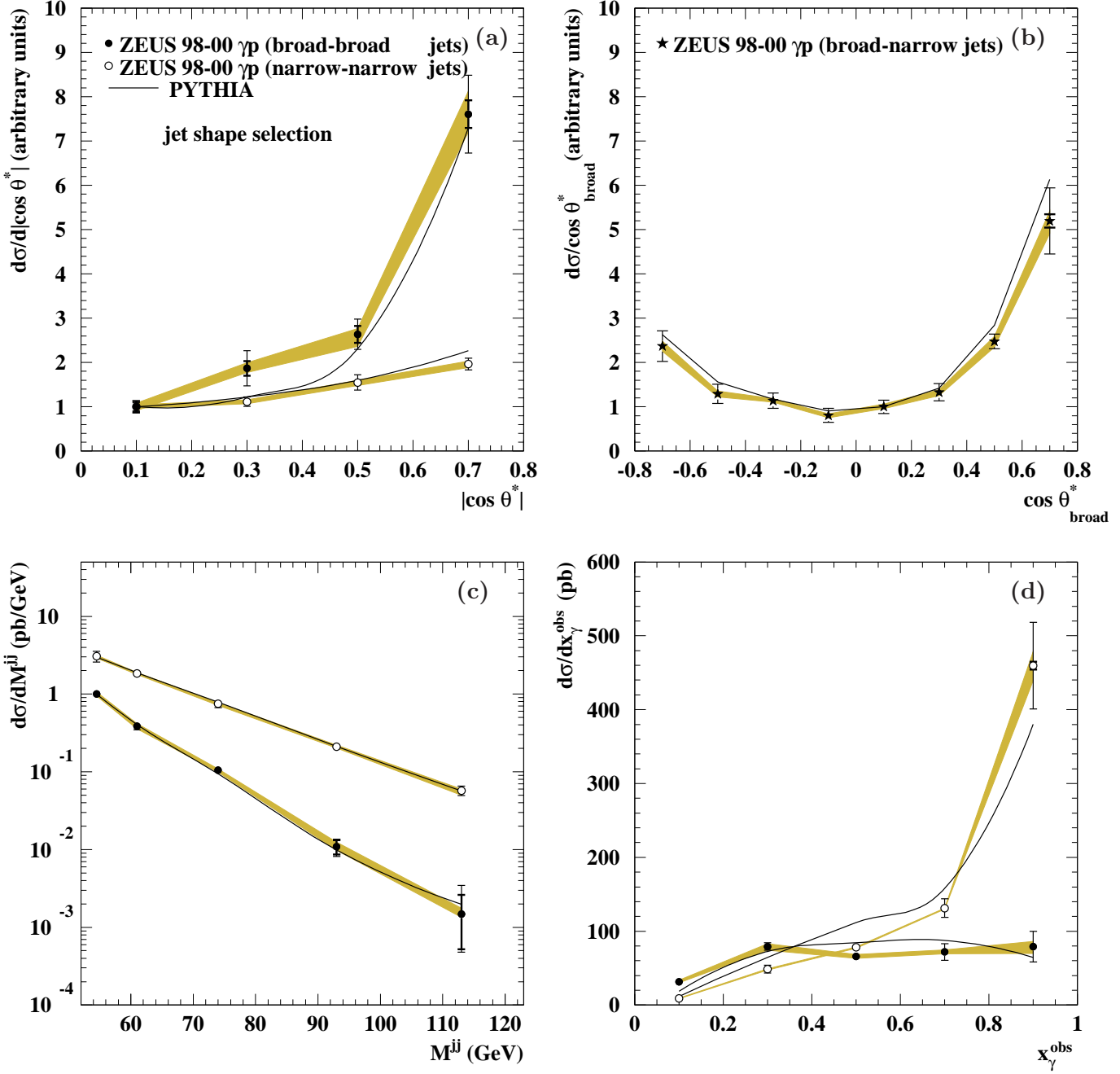


Figure 16: Measured differential ep cross sections for dijet photoproduction with $E_T^{\text{jet}1} > 17 \text{ GeV}$, $E_T^{\text{jet}2} > 14 \text{ GeV}$ and $-1 < \eta^{\text{jet}} < 2.5$ in the kinematic region defined by $Q^2 < 1 \text{ GeV}^2$ and $142 < W_{\gamma p} < 293 \text{ GeV}$ as a function of (a) $|\cos\theta^*|$ and (b) $\cos\theta^*_{\text{broad}}$ for $M^{\text{jj}} > 52 \text{ GeV}$, (c) M^{jj} for $|\cos\theta^*| < 0.8$ and (d) x_{γ}^{obs} . The cross sections are for events with broad-broad (dots), narrow-narrow (open circles) and broad-narrow (stars) dijet configurations selected according to their shape. Other details are as in the caption to Fig. 13.

ZEUS

